Pparα and fatty acid oxidation coordinate hepatic transcriptional architecture.

Running title: Fatty acids alter the epigenome.

Kyle S. Cavagnini,[1] and Michael J. Wolfgang[1,2,3*]

[1]Department of Biological Chemistry, [2] Pharmacology and Molecular Sciences,

The Johns Hopkins University School of Medicine, Baltimore, Maryland.

[3]Lead Contact

*Address correspondence to**: Michael J. Wolfgang, Ph.D.,** Department of Biological Chemistry, Johns Hopkins University School of Medicine, 855 N. Wolfe St., 475 Rangos Building, Baltimore, MD 21205, Tel: 443-287-7680, Email: mwolfga1@jhmi.edu

HIGHLIGHTS

- Fasting-induced transcription and histone acetylation are largely independent of acetyl-CoA concentration.
- Deficits in fatty acid oxidation prompt epigenetic changes and Pparα-sensitive transcription.
- Fasting prompts enhancer priming and acetylation proximal to Pparα binding sites independent of Pparα.
- Patterns of Pparα target genes can be distinguished by epigenetic marks at promoters and enhancers.

ABSTRACT

Fasting requires tight coordination between the metabolism and transcriptional output of hepatocytes to maintain systemic glucose and lipid homeostasis. Genetically-defined deficits in hepatic fatty acid oxidation result in dramatic fasting-induced hepatocyte lipid accumulation and induction of genes for oxidative metabolism, thereby providing a mouse model to interrogate the mechanisms by which the liver senses and transcriptionally responds to fluctuations in lipid levels. While fatty acid oxidation is required for a rise in acetyl-CoA and subsequent lysine acetylation following a fast, changes in histone acetylation (total, H3K9ac, and H3K27ac) associated with transcription do not require fatty acid oxidation. Instead, excess fatty acids prompt induction of lipid catabolic genes largely via ligand-activated Pparα. We observe that active enhancers in fasting mice are enriched for Pparα binding motifs, and that inhibition of hepatic fatty acid oxidation results in elevated enhancer priming and acetylation proximal to Pparα binding sites within regulatory elements largely associated with genes in lipid metabolism. Also, a greater number of Pparα-associated H3K27ac signal changes occur at active enhancers compared to promoters, suggesting a genomic mechanism for Pparα to tune target gene expression levels. Overall, these data demonstrate the requirement for Pparα activation in maintaining transcriptionally permissive hepatic genomic architecture particularly when fatty acid oxidation is limiting.

INTRODUCTION

The liver is a principle regulator of systemic lipid physiology. In this role the hepatocyte requires signaling mechanisms by which to sense and respond to fluctuations in lipid availability. This is especially important during periods of nutrient deprivation, such as fasting (George, 2006). Fasting stimulates fatty acid mobilization from adipose, whereby they are taken up and broken down in the liver via mitochondrial β-oxidation to provide hepatocytes with ATP, NADH, and acetyl-CoA (Stern et al., 2016; The and Schulz, 1991). Errors in these fundamental catabolic

52 processes result in metabolic aberrations, such as fasting hypoketotic-hypoglycemia, and can
53 also contribute to the pathogenesis and progression of conditions such as diabetes, obesity,
54 and chronic liver disease (Asrani et al., 2019; Gong et al., 2017; Houten et al., 2016; Ponziani et
55 al., 2015).

56 The nuclear hormone receptor peroxisome proliferator-activated receptor alpha (Pparα)
57 plays a governing role in regulating hepatic lipid homeostasis and is thus a key component of
58 the fasting response (Kersten, 2014; Kersten et al., 1999; Leone et al., 1999). Upon activation
59 by lipid ligands, such as long chain fatty acids, Pparα and its heterodimer partner retinoid X
60 receptor alpha (RXRα) will bind to DNA and effect transcription of target genes (Bardot et al.,
61 1993; Boergesen et al., 2012; Evans and Mangelsdorf, 2014; Gearing et al., 1993). This
62 transcriptional program includes genes for mitochondrial and peroxisomal β-oxidation,
63 microsomal ω-oxidation, and ketogenesis (Aoyama et al., 1998; Mandard et al., 2004;
64 Rakhshandehroo et al., 2009). It prompts induction of regulators for mitochondrial metabolism
65 such as carnitine palmityltransferase 1a (*Cpt1a*) and pyruvate dehydrogenase kinase 4 (*Pdk4*),
66 which respectively promote mitochondrial fatty acid import and inhibit pyruvate oxidation,
67 (Huang et al., 2002; Song et al., 2010; Wu et al., 2001). Pparα also activates transcription of
68 pro-catabolic hepatokines such as fibroblast growth factor 21 (*Fgf21*), which help mediate the
69 adaptive starvation response systemically (Inagaki et al., 2007; Iroz et al., 2017). Pparα
70 knockout mice display diminished transcription of these and other genes for oxidative
71 metabolism, which over time contributes to hepatic lipid accumulation and steatosis (Aoyama et
72 al., 1998; Kersten et al., 1999; Leone et al., 1999; Reddy, 2001; Ruppert et al., 2019).

73 Transcription factor binding hubs, such as promoters and enhancer elements, play a
74 fundamental role in regulating hepatic transcription (Goldstein and Hager, 2015; Jump et al.,
75 2013; Karagianni and Talianidis, 2015; Qin et al., 2020). Enhancers are cis-regulatory genetic
76 elements that facilitate transcription initiation and processivity; they are classified as silenced,
77 poised, or active (Creyghton et al., 2010). Poised enhancers are marked by enrichment of

78 epigenetic modifications including H3K4me1 and H3K27me3 (Calo and Wysocka, 2013; Heinz
79 et al., 2015). Active enhancers are marked by a coincidence of H3K4me1 and H3K27ac, as
80 well as increased chromatin accessibility and the presence of histone acetyltransferases such
81 as p300 (Andersson and Sandelin, 2020; Creyghton et al., 2010; Raisner et al., 2018). The
82 hepatic fasting response requires careful balance between gluconeogenesis and ketogenesis.
83 The interplay between each process is in part governed by transcription factor binding patterns,
84 including changes in the active enhancer landscape. Glucocorticoid receptor (GR)-assisted
85 loading of cAMP responsive element binding protein I promotes activation of gluconeogenic
86 enhancers (Goldstein et al., 2017). In contrast, ketogenic enhancers are proposed to have a
87 more gradual enhancer maturation which is correlated to GR-stimulated expression of Pparα
88 and increased chromatin accessibility in proximity to Pparα binding motifs (Goldstein et al.,
89 2017). Moreover, Pparα binding has been directly detected at fasting-induced enhancers using
90 ChIP-seq (Lee et al., 2014; Sommars et al., 2019). Pparα-null mice have suppressed indicators
91 for active enhancers, including decreased enhancer RNA levels and H3K27ac ChIP-seq signal
92 (Guan et al., 2018; Sommars et al., 2019).
93 In this study we take advantage of mice with a genetically-defined deficit in hepatic fatty
94 acid oxidation to further investigate the contribution of Pparα in regulating the hepatic fasting
95 transcriptional landscape, including a close inspection of its activity at active enhancers.
96 Carnitine palmityltransferase 2 (Cpt2) is a required enzyme for the transport of long chain fatty
97 acids into the mitochondria (Houten et al., 2016). Its loss deprives the mitochondria of fatty acid
98 substrate, and it is thus an obligate enzyme for mitochondrial β-oxidation. During a fast, mice
99 with a liver-specific deletion of Cpt2 ($Cpt2^{L-/-}$) are unable to clear excess lipid (Lee et al., 2016).
100 This results in drastic fatty acid accumulation accompanied by augmented transcription of many
101 Pparα target genes (Lee et al., 2016). These mice are therefore a model of Pparα activation by
102 build-up of endogenous lipid ligands. We use this system to further explore the effect of hepatic

103 lipid sensing on gene activation, and the role for Pparα activation in maintaining transcriptionally
104 permissive chromatin. In particular we describe distinct patterns of Pparα target gene
105 transcription that are distinguished by epigenetic marks at promoters and enhancers. We
106 further observe that Pparα-sensitive enhancers are largely associated with lipid metabolism, and
107 deficits in fatty acid oxidation prompt elevated priming and acetylation at these loci. Altogether
108 our findings provide genomic insight into how fatty acids alter the epigenome to affect
109 transcription during periods of nutrient deprivation.
110

111 **RESULTS**

112 **Impaired hepatic mitochondrial fatty acid oxidation elicits putative Pparα target genes**
113 **despite a suppression in lysine acetylation.**

114 Mice lacking hepatic Cpt2 ($Cpt2^{L-/-}$) are unable to utilize long chain fatty acids for mitochondrial
115 β-oxidation. Following a fast, this results in fatty liver and dramatic induction of pro-catabolic
116 hepatic genes, thereby providing a useful genetic model to interrogate fatty-acid stimulated
117 transcription (Bowman et al., 2019; Lee et al., 2016). To fully characterize the transcriptional
118 landscape of the fasting $Cpt2^{L-/-}$ liver, we performed RNA-seq on livers harvested from 9-week
119 old wildtype (WT) and $Cpt2^{L-/-}$ mice fasted for 24 hours (**Fig. 1a, Table S1**). This expanded
120 upon our previously published observations that impaired hepatic β-oxidation is associated with
121 augmented fasting-induced transcription of genes for regulation of mitochondrial metabolism
122 (*Pdk4*), regulation of peroxisomal metabolism (*Ehhadh*), and pro-catabolic hepatokines (*Fgf21*)
123 (Lee et al., 2016). Indeed, gene ontology for all significantly upregulated transcripts ($Cpt2^{L-/-}$/WT
124 fold change ≥ 2, padj < 0.05) returned several terms for fatty acid metabolism (**Fig. S1a**). We
125 next performed TMT-based quantitative proteomics to confirm the induction of these genes at
126 the protein level (**Table S2**). We found that, in parallel to the RNA-seq data, $Cpt2^{L-/-}$ upregulated
127 peptides were enriched for gene ontology terms related to fatty acid biology (**Fig. S1b, S1c**).
128 These results provide additional evidence demonstrating that impaired β-oxidation triggers a

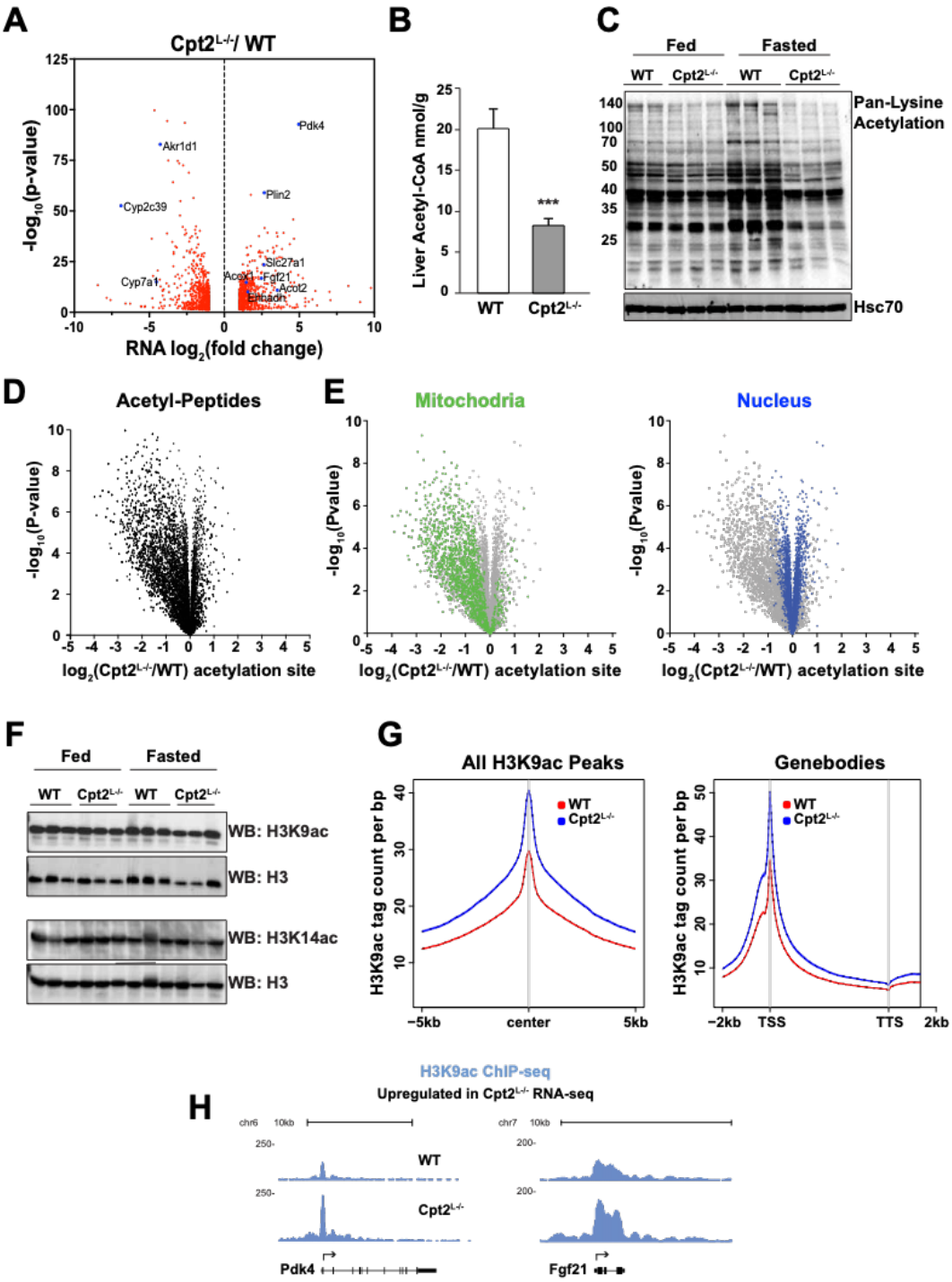

Fig 1. Fasted Cpt2$^{L-/-}$ liver exhibits deficits in lysine-acetylation along with metabolic gene induction.

A. Volcano plot displaying differentially expressed transcripts (fold change ≥ |2|, padj < 0.05) between 24hr fasted WT and Cpt2$^{L-/-}$ liver as determined by RNA-seq (n=4).
B. Tissue acetyl-CoA concentration from 24hr fasted WT and Cpt2$^{L-/-}$ liver (n=6, mean ± SEM). Significance determined using Student two-tailed t test, ***p < 0.001.
C. Western blot for acetyl-lysine and HSC70 loading control in fed and fasted WT and Cpt2$^{L-/-}$ livers.
D. Volcano plots showing magnitude and significance for fasted liver acetyl-proteome, measured by TMT-based quantitative mass spectrometry (n=5).
E. Volcano plots showing magnitude and significance for mitochondrial acetyl-proteome and nuclear acetyl-proteome.
F. Representative Western blot of acid-precipitated histones from fed and fasted WT and Cpt2$^{L-/-}$ liver tissue.

(*legend continued on next page)*

Fig 1. Fasted Cpt2$^{L-/-}$ liver exhibits deficits in lysine-acetylation along with metabolic gene induction.

G. Aggregation plot depicting liver H3K9ac ChIP-seq mean tag density for (*left*) all H3K9ac ChIP-seq peak centers with ±5kb flanking regions and (*right*) across all gene bodies with ±2kb flanking regions. TSS = transcription start site, TTS = transcription termination site. n=1
H. H3K9ac ChIP-seq genome browser tracks for representative genes that are upregulated in Cpt2$^{L-/-}$ RNA-seq, showing increased ChIP-seq signal in the fasted Cpt2$^{L-/-}$ liver.

130 compensatory transcriptional program in an attempt to relieve the lipid burden, a process which
131 includes shuttling fatty acids into other metabolic pathways such as peroxisomal oxidation.
132 Others have suggested that fatty acid oxidation promotes transcription for lipid
133 catabolism via histone acetylation from fatty acid-derived acetyl-CoA (McDonnell et al., 2016).
134 We observed that Cpt2$^{L-/-}$ mice exhibited suppressed hepatic acetyl-CoA concentration and
135 failed to induce protein acetylation following a fast, which therefore allowed us to examine this
136 hypothesis *in vivo* (**Fig. 1b, 1c**). To gain a more granular view of the proteins that exhibited
137 hypoacetylation, we mapped and quantified protein acetylation via TMT-based mass
138 spectrometry (**Fig. 1d, Table S3)**. We found that mitochondrial protein acetylation was
139 suppressed in Cpt2$^{L-/-}$ mice as expected due to a lack of mitochondrial β-oxidation (**Fig. 1e,**
140 **S1e**). In fact, lysine acetylation was globally reduced in Cpt2$^{L-/-}$ mice with the noted exception of
141 nuclear peptides, which retained comparable levels of acetylation between WT and Cpt2$^{L-/-}$ mice
142 (**Fig. 1e, S1d**). These data indicate that the deficit in mitochondrial β-oxidation limits liver
143 acetyl-CoA substrate for lysine acetylation, with the exception of the nucleus where acetyl-lysine
144 levels appear buffered.
145 Analysis of acetyl-histone peptides provides evidence against bulk histone acetylation as
146 a primary driver of transcriptional activation. 91 unique acetyl-histone peptides were detected in
147 the acetyl-proteome, of which none were hyperacetylated, 38.5% were hypoacetylated and the
148 remaining 61.5% showed no significant change to acetylation state between Cpt2$^{L-/-}$ and WT
149 animals (**Table S3**). Consistent with those data, bulk changes in histone acetylation were not
150 observed for histone marks H3K9ac or H3K14ac (**Fig. 1f**). To gain detailed insight into fatty
151 acid oxidation-dependent histone acetylation, we next turned to ChIP-seq for H3K9ac. Global
152 H3K9ac levels were higher in Cpt2$^{L-/-}$ liver, including at gene promoters, consistent with the
153 augmented transcriptional profile of Cpt2$^{L-/-}$ mice (**Fig. 1g**). Local patterns of H3K9ac gene body

154 occupancy trended with RNA-seq fold-change (**Fig. 1h, S1f**). These data are not consistent
155 with the notion that the fatty acid oxidation-dependent generation of acetyl-CoA is a primary
156 driver of gene expression via an epigenetic mechanism, but rather point towards another lipid
157 sensing mechanism for transcriptional activation.

158 To better understand how fatty acids affect the chromatin landscape, including promotor
159 accessibility and binding motifs for transcription factors induced in fasting Cpt2$^{L-/-}$ liver, we next
160 turned to Assay for Transposase Accessible Chromatin Sequencing (ATAC-seq). ATAC-seq
161 profiles of fasted Cpt2$^{L-/-}$ and WT liver tissues were overall similar. A total of 69,485 ATAC-seq
162 sites were measured across all samples, of which 75.6% are shared by both fasted Cpt2$^{L-/-}$ and
163 WT animals (**Fig. 2a**). Cpt2$^{L-/-}$ livers had a notable increase in chromatin accessibility near
164 transcription start sites (**Fig. 2b).** Of the 9273 differentially upregulated ATAC sites (fold change
165 Cpt2$^{L-/-}$/WT ≥ +2), 16% were detected in gene promotors. Differential accessibility aligned with
166 RNA-seq trends (**Fig. 2c, S2a**). Motif analysis on ATAC peaks found at gene promotors for
167 upregulated Cpt2$^{L-/-}$ transcripts revealed Pparα and its heterodimer binding partner Rxr as the
168 top hits (**Fig. 2d**). Pparα targets are often defined by their response to a Pparα agonist, such as
169 WY-14643 (Brocker et al., 2020; Janssen et al., 2015; Lee et al., 1995; Li et al., 2018;
170 Rakhshandehroo et al., 2007). We determined that 52% of genes upregulated in Cpt2$^{L-/-}$ animals
171 are sensitive to WY-14643 (**Fig. 2e**) (Naiman et al., 2019). Together, the proteomic, acetyl-
172 proteomic, RNA-seq, ATAC-seq and H3K9ac ChIP-seq data suggest that deficits in hepatic fatty
173 acid oxidation by the loss of Cpt2 elevates endogenous lipid ligands to induce Pparα at
174 promoters of genes important for lipid catabolism despite a suppression in acetyl-CoA.
175

176 **Pparα, Cpt2$^{L-/-}$ double knockout mice demonstrate Pparα dependent and independent**
177 **transcription.**

178 Given the abundance of putative Pparα target genes and enrichment for Pparα promoter
179 binding motifs in fasted Cpt2$^{L-/-}$ livers, we decided to define the requirement for Pparα in

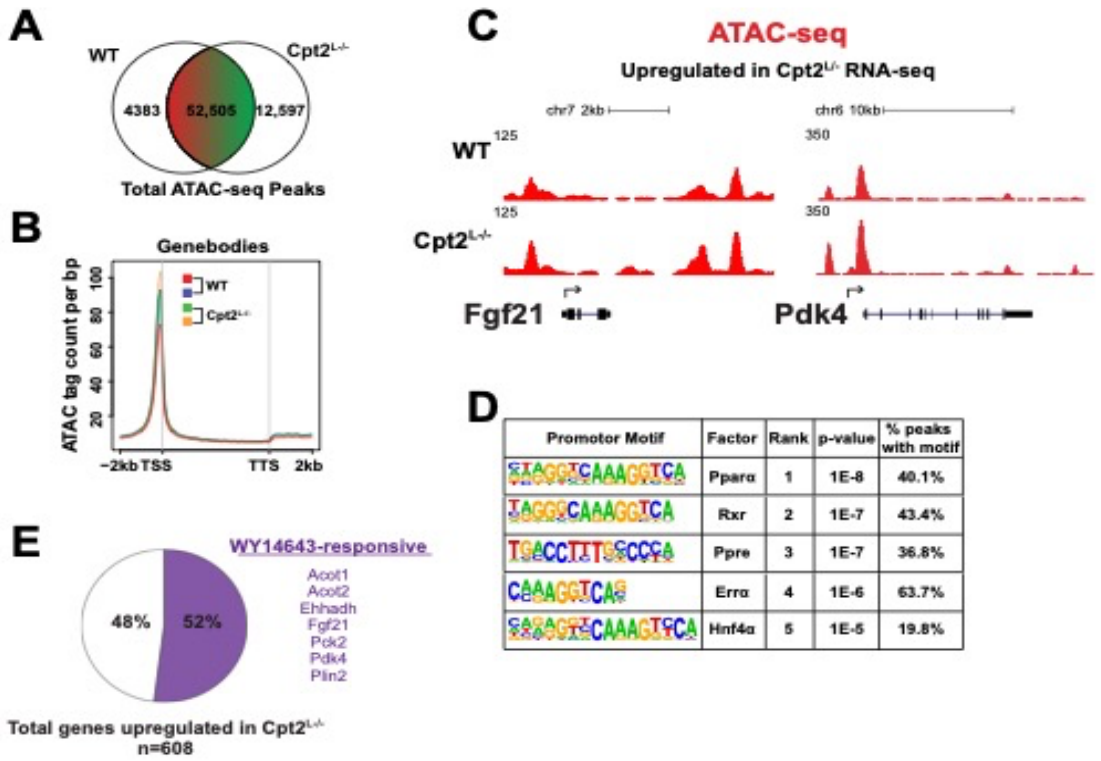

Fig 2. Fasting-induced genes in Cpt2$^{L-/-}$ liver are Pparα-responsive

A. Venn diagram showing unique and shared ATAC-seq peaks detected in fasted WT and Cpt2$^{L-/-}$ liver (n=2).
B. Aggregation plot depicting liver ATAC-seq mean tag density for all gene bodies with ±2kb flanking regions. TSS = transcription start site, TTS = transcription termination site.
C. ATAC-seq genome browser tracks for representative genes that were upregulated in Cpt2$^{L-/-}$ RNA-seq.
D. Top results from HOMER enrichment analysis for known motifs in ATAC-seq promoter peaks for genes induced in Cpt2$^{L-/-}$ liver.
E. Pie chart depicting Cpt2$^{L-/-}$ induced genes previously shown to respond to the Pparα agonist WY-14643 (GSE140063, Naiman et al., 2019) .

181 the transcriptional response of Cpt2$^{L-/-}$ mice by generating double knockout (DKO) mice.
182 Cpt2$^{L-/-}$;Pparα$^{-/-}$ DKO animals were generated using mice harboring a whole-body deletion of
183 Pparα (Pparα$^{-/-}$) bred to Cpt2$^{L-/-}$ mice. Subsequent experiments in this study were conducted
184 using 24hr fasted 9-week old WT , Cpt2$^{L-/-}$, Pparα$^{-/-}$, and DKO mice. All genotypes were viable
185 and fertile and were not associated with changes in body weight (**Fig. 3a**). We have previously
186 shown that fasted Cpt2$^{L-/-}$ mice have significantly increased liver mass due to excess fatty acids;
187 the DKO mice share this phenotype (**Fig. 3b**). While Cpt2$^{L-/-}$ mice did not exhibit differences in
188 fasting glycemia compared to controls, Pparα$^{-/-}$ and DKO mice exhibited mild fasting
189 hypoglycemia (**Fig. 3c**). This phenotype was previously described for fasted Pparα$^{-/-}$ animals
190 (Kersten et al., 1999). Pparα$^{-/-}$ mice had approximately half of the circulating fasting ketone
191 bodies such as β-hydroxybutyrate (βHB) compared to WT animals (**Fig. 3d**). However, Cpt2$^{L-/-}$
192 and DKO mice did not produce βHB following a 24hr fast, demonstrating a requirement for
193 hepatic fatty acid oxidation for ketone body generation.
194 To better understand the physiological impact of impaired hepatic β-oxidation and Pparα
195 loss, we performed global untargeted metabolomics on serum (**Fig. 3e, Table S4**). Principle
196 component analysis (PCA) showed that loss of Pparα caused broad perturbations to the serum
197 metabolome, more so than loss of Cpt2$^{L-/-}$ alone (**Fig. 3e, S3a**). This emphasizes the
198 importance of Pparα for systemic fasting physiology. These perturbations were compounded in
199 the DKO animals, which showed the greatest variation from WT controls. We've previously
200 reported that fasted Cpt2$^{L-/-}$ mice show depleted serum short- and medium-chain acyl-carnitines
201 (Lee et al., 2016). DKO mice phenocopy Cpt2$^{L-/-}$ serum levels of medium- and long-chain acyl
202 carnitines, indicating that this is likely a shared metabolic sink for the excess fatty acid in Cpt2$^{L-/-}$
203 livers (**Fig. S3b**). These data overall demonstrate that the loss of Pparα and/or the loss of
204 hepatic fatty acid oxidation result in systemic metabolic perturbations.

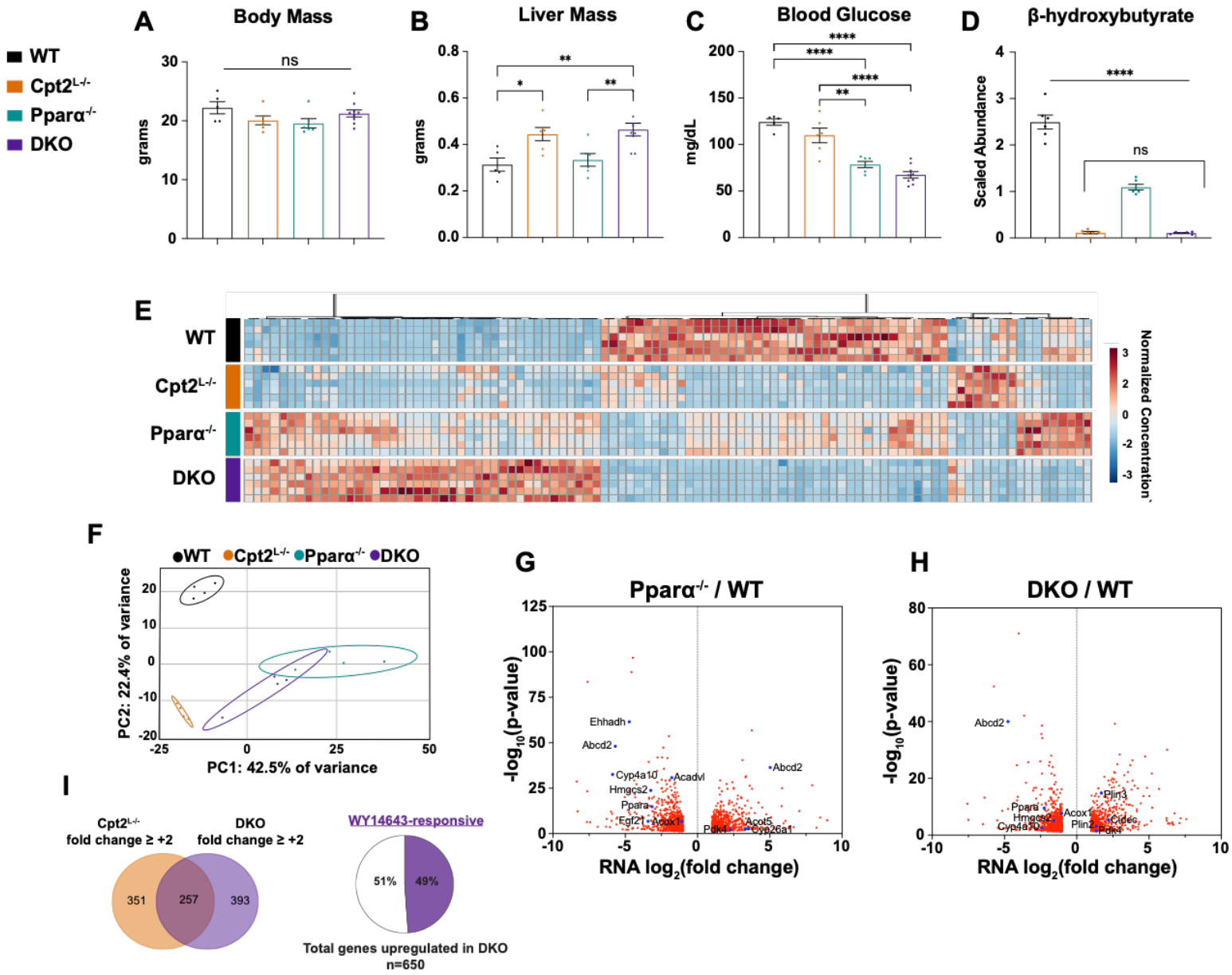

Fig 3. Pparα, Cpt2$^{L-/-}$ double knockout mice retain transcription of Pparα target genes

A. Body weight of male fasted WT, Cpt2$^{L-/-}$, Pparα$^{-/-}$, and Cpt2$^{L-/-}$;Pparα$^{-/-}$ (DKO) animals (n=6-10 mean ± SEM).
B. Wet liver weight from fasted animals (n=6-10, mean ± SEM).
C. Blood glucose from fasted animals (n=6-10, mean ± SEM).
D. Serum levels of β-hydroxybutyrate from fasted animals determined by median-scaled untargeted metabolomics (n=6, mean ± SEM).
E. Heatmap of top 100 differentially regulated serum metabolites from fasted animals (n=6).
F. Principle component analysis of RNA-seq on fasted WT, Cpt2$^{L-/-}$, Pparα$^{-/-}$, and DKO liver (n=4).
G. Volcano plot displaying RNA-seq differentially expressed transcripts between 24hr fasted WT and Pparα$^{-/-}$ livers.
H. Volcano plot displaying RNA-seq differentially expressed transcripts between 24hr fasted WT and DKO livers.
I. (*left*) Venn diagram depicting overlap between genes upregulated in Cpt2$^{L-/-}$and DKO liver compared to WT. (*right*) Pie chart depicting DKO fasting-induced genes known to respond to the Pparα agonist WY14643.

RNA-seq significance cutoff is fold change ≥ |2|, padj < 0.05. One-way ANOVA followed by Tukey's post-hoc test was performed as appropriate. *p < 0.05; **p < 0.01; ***p < 0.001; ****p < 0.0001; ns, not significant.

206 We next sought to determine the extent to which Pparα is implicated in the fasting-
207 induced Cpt2$^{L-/-}$ transcriptional response by carrying out RNA-seq on WT , Cpt2$^{L-/-}$, Pparα$^{-/-}$, and
208 DKO livers (**Table S1**). PCA of RNA-seq data revealed that the transcriptional signature for
209 Pparα$^{-/-}$ mice overlapped with that of DKO mice, while those for WT and Cpt2$^{L-/-}$ animals were
210 distinct from the other genotypes (**Fig. 3f**). There were 330 differentially expressed transcripts
211 shared between the three knockout genotypes compared to WT animals (KO/WT fold change ≥
212 |2|, padj < 0.05) (**Fig. S3c**). In line with overall transcriptional signatures, a greater number of
213 differentially expressed genes were shared between the Pparα$^{-/-}$ and DKO mice compared to
214 Cpt2$^{L-/-}$ mice. These findings are not unexpected given the central role for Pparα in regulating
215 the hepatic genes necessary for fasting oxidative metabolism.
216 The loss of Pparα alone suppressed transcription of genes for fatty acid catabolism and
217 ketogenesis, including *Ehhadh*, *Hmgcs2*, and *Fgf21* (**Fig. 3g**). Many of these genes displayed
218 blunted expression in DKO livers as well (**Fig. 3h**). Curiously, several canonical Pparα target
219 genes, such as *Plin2* and *Pdk4*, retained induction in DKO liver compared to control animals
220 (**Fig. 3h**). Further analysis of the RNA-seq data revealed that Cpt2$^{L-/-}$ and DKO animals shared
221 257 upregulated transcripts, respectively representing 42% and 40% of induced genes for those
222 genotypes (**Fig. 3i**). This suggested that there may be a transcriptional program triggered by
223 the shared metabolic perturbations presented by loss of hepatic β-oxidation. Further, 49% of
224 induced transcripts in DKO are responsive to WY-14643 (**Fig. 3i**) (Naiman et al., 2019). We
225 therefore hypothesized that a subset of genes, which are typically thought to rely upon Pparα for
226 their induction, have in addition a secondary regulatory mechanism. The limited transcription of
227 target genes that do not require Pparα is likely prompted by excess lipid burden via an
228 independent mechanism driven by Err or Hnf4α, for example.

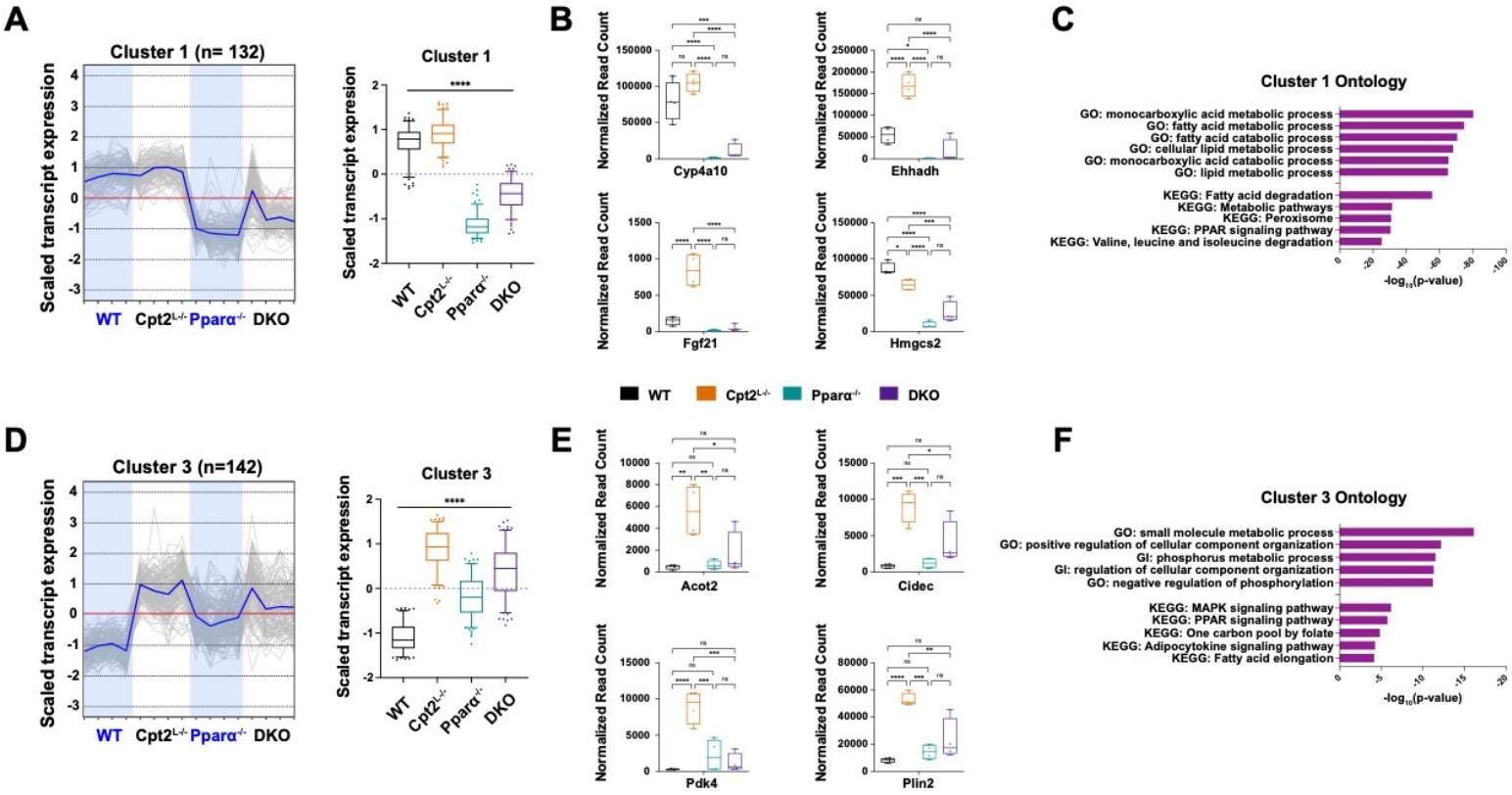

Fig 4. Unbiased clustering reveals patterns for Pparα-dependent and Pparα-independent transcription of target genes

A. *(left)* Tracing diagram of cluster 1 genes (Pparα-dependent) from fasted RNA-seq transcript levels. Blue line indicates mean expression. *(right)* Bar graph quantifying scaled transcript values. Presented as Z-score scaled transcript levels.
B. Normalized transcript read counts for select cluster 1 genes.
C. Gene ontology for cluster 1 genes ranked by significance.
D. *(left)* Tracing diagram of cluster 3 genes (Pparα-independent) from fasted RNA-seq transcript levels. Blue line indicates mean expression. *(right)* Bar graph quantifying scaled transcript values. Presented as Z-score scaled transcript levels.
E. Normalized transcript read counts for select cluster 3 genes.
F. Gene ontology for cluster 3 genes ranked by significance.

One-way ANOVA followed by Tukey's post-hoc test was performed as appropriate. *$p < 0.05$; **$p < 0.01$; ***$p < 0.001$; ****$p < 0.0001$; ns, not significant. Bar graphs represent 2%-98% percentile.

230 **Impaired hepatic fatty acid oxidation prompts distinct modes of gene regulation.**
231 We subsequently sought further resolution into the role for Pparα in regulating hepatic
232 transcription in response to impaired hepatic fatty acid oxidation, including the possibility of
233 Pparα-independent regulatory mechanisms. Unbiased k-means clustering was used to identify
234 unique patterns of gene transcription across all differentially expressed transcripts (**Fig. S4a**,
235 **Table S5**). Of the five clusters identified, two in particular (1 & 3) were associated with the
236 $Cpt2^{L-/-}$ gene induction signature (**Fig. 4a, 4d**). Notably, these two groups of transcripts display
237 significantly divergent modes of Pparα-sensitive transcription.
238 Cluster 1 genes were wholly dependent upon Pparα for their transcription, as indicated
239 by their repressed expression in $Ppar\alpha^{-/-}$ and DKO fasted liver (**Fig. 4a**). Cluster 1 genes
240 included multiple canonical Pparα targets, including *Cyp4a10*, *Ehhadh*, and *Hmgcs2* (**Fig. 4b,**
241 **S3b**). These genes are respectively implicated in Pparα regulation of ω-oxidation, peroxisomal
242 oxidation, and ketogenesis (Kersten et al., 2010). Indeed, gene ontology and KEGG pathway
243 analysis on all Cluster 1 genes returned terms related to fatty acid metabolism and Pparα
244 signaling (**Fig. 4c**). These data provide further evidence that impaired hepatic fatty acid
245 oxidation activates Pparα-dependent transcription upon fasting.
246 Cluster 3 genes were likewise induced in $Cpt2^{L-/-}$ mice in a Pparα-dependent manner.
247 However, this group differs from the previous cluster in that both Pparα-null backgrounds
248 retained baseline expression levels (**Fig. 4d**). Cluster 3 genes thus sustained transcriptional
249 activity in the absence of Pparα, yet still required the transcription factor for induction in
250 response to metabolic perturbations such as a buildup of Pparα ligands. This group included
251 canonical Pparα target genes *Acot2* and *Pdk4*, whose expression in Pparα-null animals
252 displayed no significant variation from control animals (**Fig. 4e**). KEGG pathway analysis
253 returned Ppar Signaling Pathway as a top result (**Fig. 4f**). Curiously, Cluster 3 contained
254 multiple genes associated with lipid droplets, including four members of the perilipin family

255 (*Plin1-4*) and *Cidec* (Greenberg et al., 2011). *Plin2*, *Plin4*, and *Cidec* are known Pparα targets
256 (Francque et al., 2015; Kersten et al., 2010). This suggests that modules of the Pparα
257 transcription program involve building upon pre-established Pparα-independent gene
258 expression patterns to respond to specific hepatocyte metabolic states.
259
260 **Distinct Pparα target genes retain promotor accessibility despite loss of Pparα.**
261 We next asked how these unique modes of Pparα target gene transcription were reflected at the
262 level of chromatin architecture by assessing ATAC-seq from all four genotypes. Loss of Pparα
263 drastically diminishes chromatin accessibility (**Fig. S5a**). Chromatin landscape remodeling for
264 the Pparα-null mice was expected given the transcription factor's crucial role in coordinating
265 fasting metabolism, yet the severe ATAC-seq signal depletion in gene promoter regions was
266 particularly striking (**Fig. 5a**). PCA emphasized this disparity, showing that Pparα and DKO
267 animals clustered uniquely, while WT and $Cpt2^{L-/-}$ livers overlapped substantially (**Fig. S5b**). We
268 further observed there are appreciably fewer changes in discrete peak intensities between
269 $Ppar\alpha^{-/-}$ and DKO animals compared to $Cpt2^{L-/-}$ and DKO animals (**Fig. 5b**). Together these data
270 indicate that Pparα is required for proper upkeep of fasting chromatin dynamics.
271 Cluster 1 genes, those dependent upon Pparα for their expression, exhibited a common
272 pattern of promotor chromatin accessibility that is represented by *Fgf21* (**Fig. 5c**). ATAC-seq
273 genome browser tracks indicated a higher promoter peak signal in the $Cpt2^{L-/-}$ livers compared
274 to WT; accessibility was lost under a Pparα-null background. Indeed, motif analysis on ATAC-
275 seq promotor peaks for this cluster returned Pparα and its heterodimer partner Rxrα as the top
276 two hits (**Fig 5d**). Suppressed chromatin accessibility at loci enriched for Pparα binding motifs
277 indicates the need for Pparα for proper promoter dynamics.

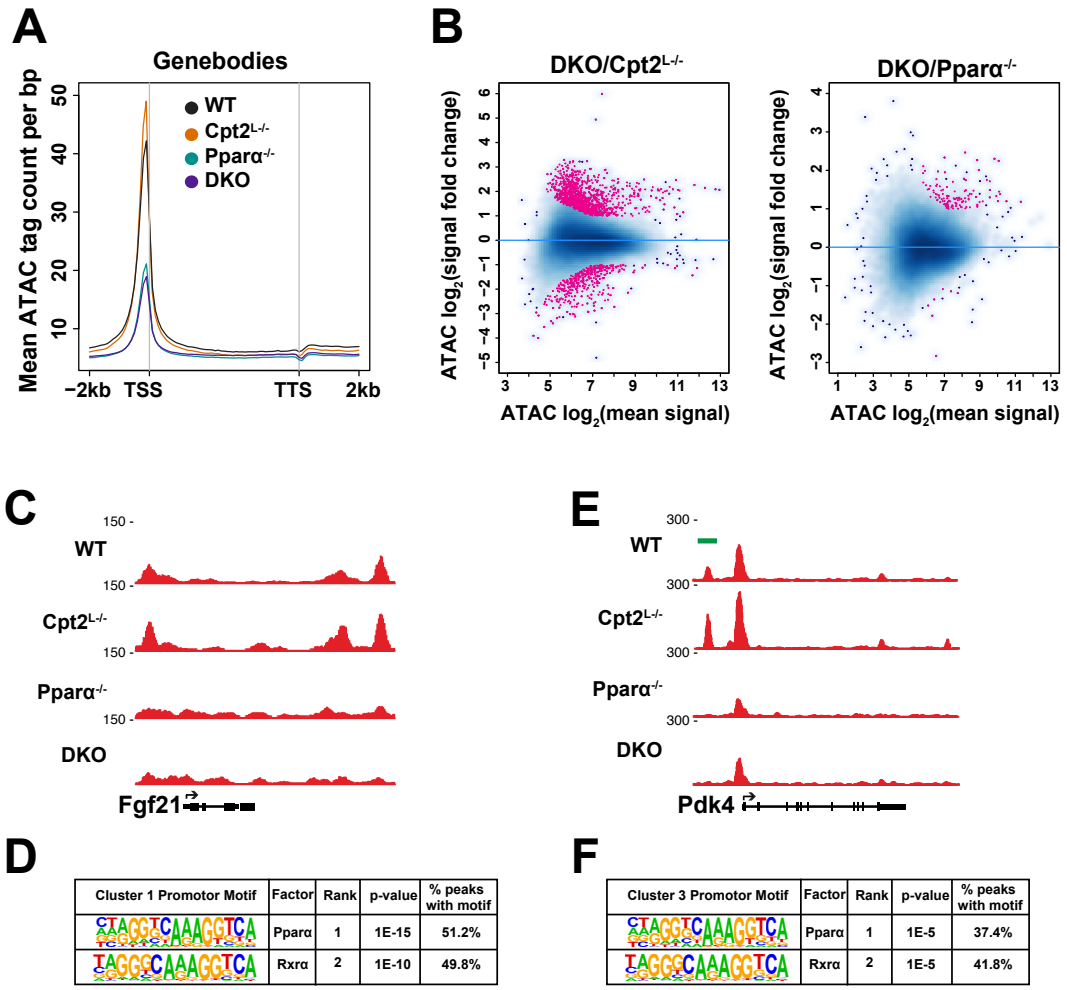

Fig 5. Loss of Pparα remodels genome-wide accessibility

A. Aggregation plot depicting liver ATAC-seq mean tag density for all gene bodies with ±2kb flanking regions in fasted WT, Cpt2$^{L-/-}$, Pparα$^{-/-}$, and DKO liver (n=2). TSS = transcription start site, TTS = transcription termination site.
B. MA plot depicting ATAC-seq differential binding analysis results between DKO/Cpt2$^{L-/-}$ and DKO/Pparα$^{-/-}$ animals. The x-axis gives the mean signal and the y-axis gives the signal fold change for a given peak. Points in pink are significant (fold change ≥ |2|, FDR < 0.05).
C. ATAC-seq genome browser tracks for cluster 1 gene *Fgf21*.
D. HOMER enrichment analysis for known motifs in ATAC-seq promoter peaks for cluster 1 genes.
E. ATAC-seq genome browser tracks for cluster 3 gene *Pdk4*. Pparα-sensitive peak interval is indicated by green bar.
F. HOMER enrichment analysis for known motifs in ATAC-seq promoter peaks for cluster 3 genes.

279 Promoter accessibility for Cluster 3 genes, those with Pparα-independent baseline
280 expression, likewise shared a common promoter chromatin architecture as illustrated by *Pdk4*
281 (**Fig. 5e**). The Cpt2$^{L-/-}$ induction pattern was once again evident in the ATAC-seq signal.
282 However, in contrast to Cluster 1 genes, this group retained a degree of promotor accessibility
283 in Pparα$^{-/-}$ and DKO mice. Interestingly, 13% of Cluster 3 genes contained an interval of open
284 promotor chromatin that was lost in both Pparα-null animals, including at the promoters for
285 Pparα targets *Acot2*, *Fabp3*, *Pdk4*, and *Plin2* (**Fig. 5e** green bar). These likely indicate binding
286 sites for Pparα directly or for another DNA regulatory protein that depends on Pparα for an
287 aspect of its activity. Cluster 3 ATAC-seq promoter peaks are enriched for Pparα and Rxrα
288 binding motifs, albeit at a lower rate than for Cluster 1 genes (**Fig. 5f**). These data together
289 indicate that Cluster 3 promoters do not require Pparα to maintain accessibility during a fast,
290 though Pparα can interact with these loci to augment target gene transcription in response to a
291 metabolic perturbation.
292
293 **Pparα-dependent and independent promotor acetylation.**
294 Differential promotor accessibility prompted questions as to how the loss of Pparα affected
295 promotor dynamics *vis a vis* histone acetylation. We therefore performed ChIP-seq for
296 H3K27ac, a histone mark generally found at active chromatin (Andersson and Sandelin, 2020).
297 H3K27ac signal was comparable between genotypes, however Cpt2$^{L-/-}$ and DKO livers
298 displayed higher H3K27ac signal near transcription start sites compared to the WT and Pparα$^{-/-}$
299 animals (**Fig. 6a, S6a**). PCA showed that WT and Cpt2$^{L-/-}$ H3K27ac distributions were distinct
300 from one another, while Pparα$^{-/-}$ and DKO animals clustered together (**Fig. 6b**). This is the
301 inverse of the ATAC-seq PCA, in which WT and Cpt2$^{L-/-}$ animals were grouped and Pparα$^{-/-}$ and
302 DKO animals were separated (**Fig. S5b**). These data indicate that the metabolic perturbations
303 in Cpt2$^{L-/-}$ and DKO livers stimulate a common configuration of H3K27ac occupancy regardless

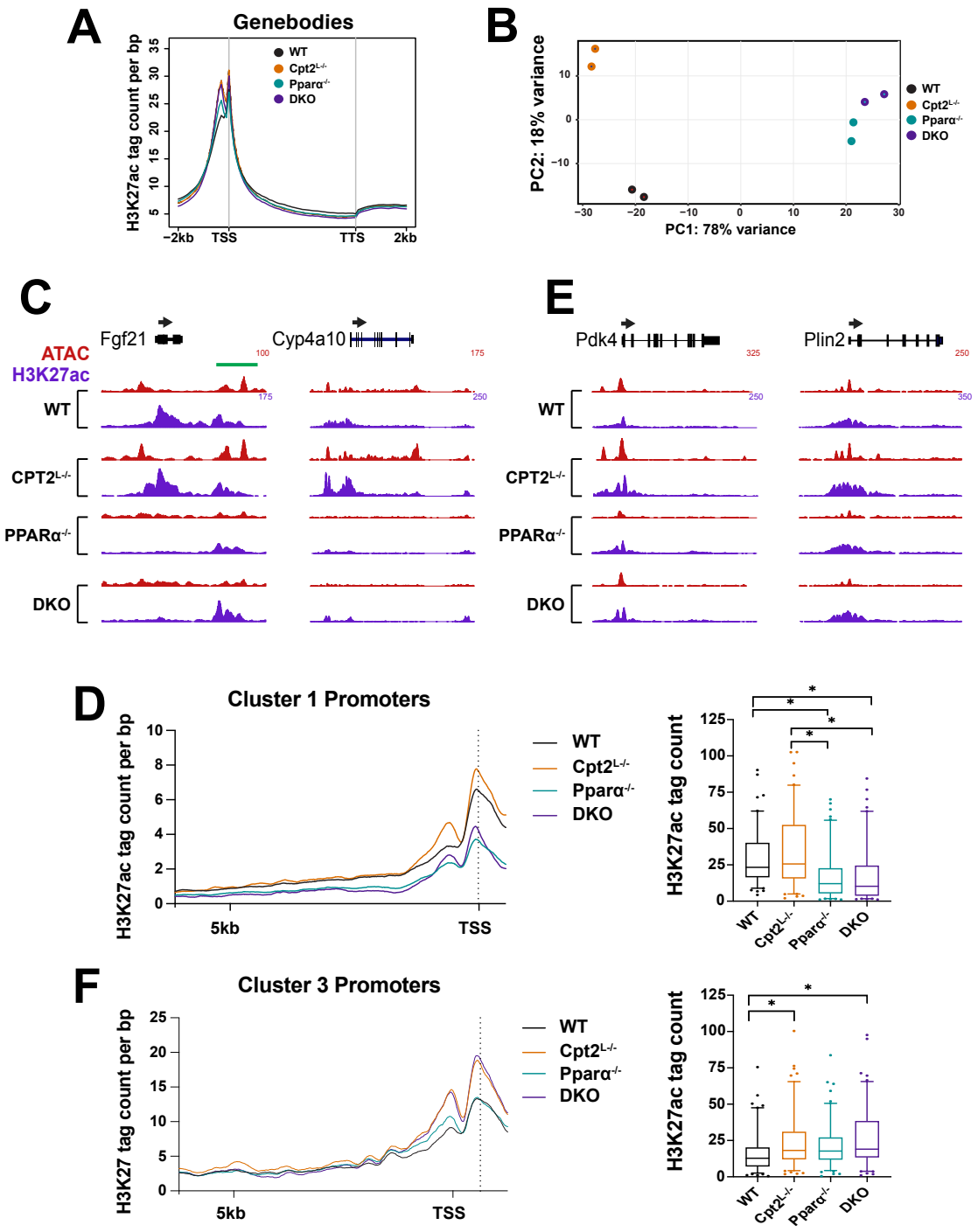

Fig 6. Differential H3K27ac occupancy patterns at Pparα target genes

A. Aggregation plot depicting liver H3K27ac ChIP-seq mean tag density for all gene bodies with ±2kb flanking regions in fasted WT, Cpt2$^{L-/-}$, Pparα$^{-/-}$, and DKO liver (n=2). TSS = transcription start site, TTS = transcription termination site.
B. PCA of H3K27ac ChIP-seq data from fasted WT, Cpt2$^{L-/-}$, Pparα$^{-/-}$, and DKO liver.
C. Genome browser track for cluster 1 genes *Fgf21* and *Cyp4a10*. ATAC-seq is presented in red, H3K27ac ChIP-seq is presented in purple. Green bar indicates downstream regulatory region.
D. (*left*) Aggregation plot for H3K27ac ChIP-seq mean tag density for cluster 1 gene promoters. (*right*) Bar graph quantifying mean values of H3K27ac ChIP-seq peaks found in cluster 1 gene promoters.
E. Genome browser track for cluster 3 genes *Pdk4* and *Plin2*. ATAC-seq is presented in red, H3K27ac ChIP-seq is presented in purple.
F. (*left*) Aggregation plot for H3K27ac ChIP-seq mean tag density for cluster 3 gene promoters. (*right*) Bar graph quantifying mean values of H3K27ac ChIP-seq peaks found in cluster 3 gene promoters.

Significance determined by Kruskal-Wallis test with Dunn's post hoc correction. *p < 0.0001; ns, not significant. Bar graphs represent 2%-98% percentile.

305 of overall chromatin accessibility. This further demonstrates lipid-driven selective histone
306 acetylation despite absence of mitochondrial β-oxidation. Pparα is not required for this
307 H3K27ac deposition, however Pparα is still needed to promote chromatin accessibility and
308 ultimately transcription of lipid catabolic genes. Comparing the WT and Cpt2$^{L-/-}$ ATAC-seq and
309 H3K27ac ChIP-seq peaksets provides additional evidence that the Cpt2$^{L-/-}$ epigenetic program
310 builds upon the baseline fasting chromatin architecture to exaggerate an established response.
311 Clusters 1 and 3, together comprising the genes induced in Cpt2$^{L-/-}$ liver, provided a
312 useful contrast to understand variations in active chromatin acetylation and how they relate to
313 Pparα. H3K27ac occupancy at Cluster 1 gene promotors paralleled ATAC-seq trends in that
314 loss of Pparα was associated with significantly decreased promoter H3K27ac tag density, as
315 indicated by *Fgf21* and *Cyp4a10* (**Fig. 6c**). There was no statistical difference in H3K27ac
316 signal between WT and Cpt2$^{L-/-}$ animals (**Fig. 6d**). At Cluster 3 gene promoters, in contrast to
317 Cluster 1, Pparα loss was not associated with depleted promoter H3K27ac signal. H3K27ac
318 occupancy was instead distinctly independent of Pparα, as indicated by its canonical target
319 genes *Pdk4* and *Plin2* (**Fig 6e**). Moreover, the Cpt2$^{L-/-}$ background is associated with
320 significantly elevated H3K27ac promoter tag density compared to WT and Pparα$^{-/-}$ animals (**Fig.
321 6f**). These observations continue to demonstrate that the lipid-associated changes in chromatin
322 accessibility are linked to site-specific epigenetic modifications in gene promoters.
323 At Cluster 1 gene *Fgf21* we noticed an acetylation pattern indicative of a regulatory
324 region downstream from the transcription termination site (**Fig. 6c**, green bar). The H3K27ac
325 signal at this site was comparable between the four genotypes, yet accessibility was only
326 observed in the WT and Cpt2$^{L-/-}$ animals. Both ATAC-seq peaks contained Pparα binding
327 motifs. This chromatin pattern parallels that observed at cluster 3 gene promoters. We
328 speculate that at these loci Pparα is able to detect antecedent chromatin acetylation as part of

329 its DNA binding mechanism, or that an epigenetic reader detects that mark and subsequently
330 loads Pparα onto chromatin, thereby promoting a transcriptionally permissive state.
331
332 **Loss of Pparα selectively alters the hepatic fasting enhancer landscape.**
333 Fasting stimulates a cascade of transcription factor loading and binding onto hepatic enhancers
334 (Goldstein et al., 2017). Enhancers can be categorized as either poised or active. The former
335 are indicated by the histone modification H3K4me1, and the latter are defined by co-occupancy
336 of H3K4me1 and H3K27ac (Creyghton et al., 2010). We decided to use the $Cpt2^{L-/-}$ model as a
337 handle by which to investigate lipid-responsive enhancer elements, and the extent to which
338 Pparα regulates both their poising and activation. A total of 8998 active enhancers were
339 detected across all genotypes (**Fig. 7a, Table S6**). Strikingly, Pparα-null animals had
340 diminished chromatin accessibility over active enhancer elements (**Fig. S7a**). Loss of either
341 Cpt2 or Pparα alone did not impact H3K4me1 density at active enhancers, but their combined
342 deletion in DKO liver reduced global enhancer priming (**Fig. 7a**). Enhancer H3K27ac signal did
343 not differ between $Ppar\alpha^{-/-}$ and WT animals. However, loss of hepatic Cpt2 was associated with
344 overall decreased H3K27ac occupancy at active enhancers. This was an unanticipated contrast
345 to increased acetylation at gene promoters under the $Cpt2^{L-/-}$ background (**Fig. 1g, 6a**). Overall
346 these data imply that while loss of Pparα alone does not negatively impact the enhancer
347 epigenetic landscape during the latter stages of a fast, global enhancer accessibility is
348 significantly hindered without the transcription factor.
349 Active enhancers were highly enriched for Hnf4α and Pparα binding motifs (**Fig. 7b**).
350 Surprisingly, Pparα ChIP-seq sites located within enhancers showed elevated H3K4me1 and
351 H3K27ac signals in all knockout genotypes (**Fig. 7c**) (Sommars et al., 2019). There was no
352 difference in enhancer H3K4me1 signal between $Cpt2^{L-/-}$ and $Ppar\alpha^{-/-}$ liver, though loss of both
353 genes in DKO animals caused significantly increased methylation near Pparα binding sites.

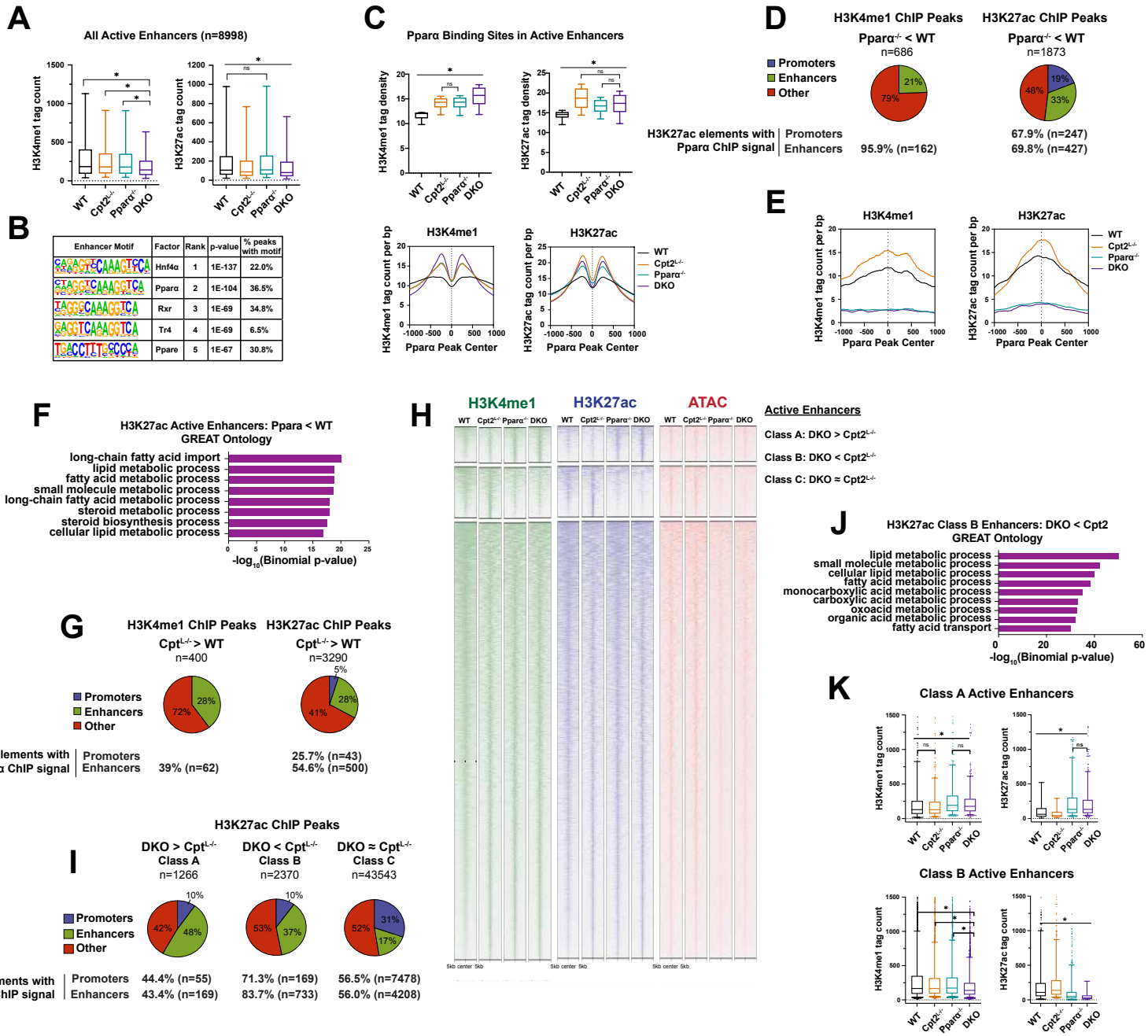

Fig 7. Lipid-sensitive enhancer elements are primed for Pparα.

A. Bar graph depicting H3K4me1 and H3K27ac tag counts at active enhancer elements.
B. HOMER motif analysis for all active enhancers as defined by H3K4me1 and H3K27ac co-occupancy.
C. (*top*) Bar graphs depicting H3K4me1 and H3K27ac mean tag density proximal to Pparα ChIP-seq binding sites in all active enhancers (±500bp from Pparα ChIP peak center). (*bottom*) Aggregation plot for H3K4me1 and H3K27ac tag density within 1kb flanking regions of Pparα ChIP peak center. (Pparα ChIP-seq: GSE118788, Sommars et al., 2019)
D. (*top*) Pie chart showing genomic distribution (promoters, enhancers, other) of H3K4me1 and H3K27ac differential peak analysis at enhancers with repressed H3K27ac signal in Pparα liver compared to WT. Promoters were not considered for H3K4me1 ChIP-seq. (*bottom*) Percent overlap between peak genomic annotation and Pparα ChIP-seq coordinates.

(legend continued on next page)

E. Aggregation plots for H3K4me1 and H3K27ac tag density within 1kb flanking regions of Pparα ChIP peak center at enhancers with repressed H3K27ac signal in Pparα liver.
F. H3K27ac GREAT ontology for enhancers with repressed H3K27ac signal in Pparα liver.
G. (*top*) Pie chart showing genomic distribution of H3K4me1 and H3K27ac differential peak analysis for enhancers with increased H3K27ac signal in $Cpt2^{L-/-}$ liver compared to WT. (*bottom*) Percent overlap between peak genomic annotation and Pparα ChIP-seq coordinates.
H. Heatmap of normalized H3K27ac ChIP-seq (purple), H3K4me1 ChIP-seq (green), and ATAC-seq (red) signal at active enhancers classified according to DKO/$Cpt2^{L-/-}$ differential peak analysis. Coverage is calculated from peak center with ±5kb flanking regions.
I. (*top*) Pie chart showing genomic distribution of H3K27ac differential peak analysis for enhancers with increased, repressed, and unchanged H3K27ac signal in DKO liver compared to $Cpt2^{L-/-}$. *(bottom*) Percent overlap between peak genomic annotation and Pparα ChIP-seq coordinates.
J. H3K27ac GREAT ontology for Class B enhancers (DKO < $Cpt2^{L-/-}$).
K. Bar graphs quantifying normalized H3K27ac and H3K4me1 ChIP-seq signal at Class A and Class B active enhancers

Significance determined by Kruskal-Wallis test with Dunn's post hoc correction. *p < 0.0001; ns, not significant. Bar graphs represent 2%-98% percentile.

H3K27ac tag density flanking Pparα binding sites was increased in $Cpt2^{L-/-}$ animals compared to Pparα$^{-/-}$. $Cpt2^{L-/-}$ animals also had increased ATAC-seq signal over Pparα enhancer sites compared to WT animals (**Fig. S7b**). As might be expected, chromatin accessibility over Pparα sites was decreased in Pparα-null livers, though this was despite increased enhancer priming and acetylation over WT baselines at those loci (**Fig. 7c, S7b**). This indicates that the active epigenetic state is maintained independent of Pparα at these enhancers, but Pparα is required to promote chromatin accessibility. Together these data show that perturbations to fatty acid catabolism are associated with amplified enhancer priming and acetylation specifically near Pparα binding sites even in the absence of the transcription factor. We propose this is an epigenetic mechanism for the hepatocyte to prime a genomic response to impaired lipid catabolism.

We next examined the specific changes to enhancer state at loci that are differentially regulated in Pparα$^{-/-}$ liver compared to WT. Loss of Pparα was associated with targeted repression of H3K27ac signal, and to a lesser extent H3K4me1 signal (**Fig. 7d**). Only 169 enhancers had suppressed priming in Pparα$^{-/-}$ animals in contrast to the 612 enhancers with suppressed H3K27ac signal in Pparα$^{-/-}$ animals. As expected, these downregulated regions

371 contained a high frequency of Pparα ChIP-seq binding sites. Curiously, 33% of H3K27ac peaks
372 repressed in Pparα$^{-/-}$ liver were located within enhancer elements, while only 19% of H3K27ac
373 signal changes were found in gene promoters (**Fig. 7d**). In other words, loss of Pparα
374 diminished chromatin acetylation at a greater number of enhancers than promoters. Enhancers
375 with blunted acetylation in Pparα$^{-/-}$ liver displayed highly enriched H3K4me1 and H3K27ac
376 signals in Cpt2$^{L-/-}$ animals (**Fig. 7e**). The Genomic Regions Enrichment of Annotations Tool
377 (GREAT), which provides ontologies for enhancer function using a binomial test specific for
378 long-range genomic regulatory domains, showed that enhancers repressed by loss of Pparα
379 were associated with ontology terms for fatty acid metabolism (**Fig. 7f**) (McLean et al., 2010).
380 These data are consistent with a model in which Cpt2 loss drives Pparα signaling, and that
381 Pparα target gene transcription is associated with heightened activation of enhancers
382 associated with lipid metabolism.
383 Following up on these observations, we next examined how a deficit in β-oxidation
384 affected the hepatic enhancer landscape, and the extent to which Pparα is implicated in
385 genomic maintenance under these metabolic conditions. Loss of Cpt2 had minimal effects on
386 overall enhancer priming (**Fig. 7g**). In contrast, Cpt2$^{L-/-}$ mice had 915 enhancer regions with
387 increased H3K27ac signal. 55% of these regions contain Pparα binding sites. Indeed, Cpt2$^{L-/-}$
388 animals had a prominent increase in both enhancer priming and acetylation over Pparα ChIP
389 sites (**Fig. S7c**). At these Cpt2$^{L-/-}$-sensitive loci we also observed increased H3K4me1 and
390 H3K27ac ChIP signals over Pparα binding sites in Pparα-null animals compared to WT controls,
391 indicating that enhancers with epigenetic sensitivity to impaired β-oxidation likewise respond to
392 impaired Pparα signaling, perhaps designating a response to drive augmented transcription
393 such as we see in the Cpt2$^{L-/-}$ mice (**Fig. S7c**).
394 The DKO mice clarify the role for Pparα at these enhancer elements. These mice had a
395 striking change to their active enhancer landscape when compared to their Cpt2$^{L-/-}$counterparts.

396 We initially noticed there were far fewer changes in enhancer priming compared to changes in
397 enhancer acetylation (**Fig. 7i, S7d**). A total of 1487 differentially regulated enhancers were
398 detected between the two genotypes, which were broken down into three groups according to
399 differential H3K27ac ChIP signal (**Fig. 7h**). Class B enhancers (n=876) were defined by
400 statistically significant H3K27ac depletion in DKO mice compared to Cpt2$^{L-/-}$ (**Fig. 7h, 7k**). We
401 consider these to be the enhancer elements at which the ligand-activated Pparα signaling
402 program specifically impacts acetylation in response to lipid sensing. The high incidence of
403 Pparα binding sites within these enhancers suggests that Pparα itself plays a direct role in local
404 H3K27ac deposition (**Fig. 7i**). Cpt2$^{L-/-}$ animals had increased H3K27ac signal at these regions
405 compared to WT (**Fig. 7k**). We further noted that loss of Pparα on the Cpt2$^{L-/-}$ background had
406 an outsized effect on enhancer acetylation compared to promoter acetylation (**Fig. 7i**). Finally,
407 GREAT analysis indicates that proximal genes for Class B enhancers were associated with
408 multiple lipid gene ontology terms (**Fig. 7j**). Together these data demonstrate the substantial
409 role for enhancer elements in the Pparα transcriptional response, and that lipid-amplified Pparα
410 signaling is perhaps mediated more substantially by epigenetic changes to enhancer regions
411 than at promoters.

412 Class A enhancers (n=611) were defined by a greater than two-fold increase in H3K27ac
413 signal in DKO mice compared to Cpt2$^{L-/-}$ liver. DKO Class A enhancer acetylation was similarly
414 increased over WT animals (**Fig. 7k**). This augmented H3K27ac signal was shared by Pparα$^{-/-}$
415 animals. Likewise, both Pparα$^{-/-}$ and DKO animals displayed elevated H3K4me1 priming levels
416 at Class A enhancers (**Fig. 7k**). This implies Pparα loss is associated with enhancer activation
417 that may be linked to other metabolic processes. Class C enhancers (n=7511), which showed
418 no change in acetylation state between Cpt2$^{L-/-}$ and DKO animals, represent 83% of the active
419 enhancer landscape (**Fig. S7e**), emphasizing that the genomic perturbations presented by loss
420 of Cpt2 or Pparα result in specific, targeted changes to enhancer epigenetic state.

421 Altogether these data demonstrate that metabolic perturbations such as inhibiting
422 hepatic fatty acid oxidation or loss of Pparα result in higher levels of enhancer priming and
423 acetylation proximal to Pparα sites that are largely associated with lipid metabolism. Pparα
424 DNA binding is proceeded by enhancer priming and acetylation. This is clearly illustrated at
425 Pparα-bound enhancers found near *Fgf21* and *Pdk4* (**Fig. S7f**). The acetylation may even be
426 the signal for Pparα to engage these regulatory elements. Furthermore, while changes to
427 enhancer epigenetic state are more localized near Pparα binding sites, the transcription factor is
428 so crucial to maintaining permissive chromatin that loss of Pparα repressed chromatin
429 accessibility across the global enhancer network. We also surmise that changes to the
430 enhancer landscape comprise a significant component of ligand-activated Pparα signaling, with
431 quantitatively more Pparα-associated changes in acetylation occurring at enhancers compared
432 to promoters. Overall, these data show the requirement for Pparα activation in maintaining
433 transcriptionally permissive hepatic genomic architecture, particularly when the hepatocyte must
434 sense and respond to elevated lipid.
435

436 **DISCUSSION**

437 A foundational question in liver metabolism is how the hepatocyte senses and responds to
438 fluctuations in lipid availability. This ultimately requires tight coordination between the
439 hepatocyte's metabolic state, genome architecture, and transcriptional output. Fasting $Cpt2^{L-/-}$
440 mice prompts accumulation of fatty acids, including putative endogenous Pparα ligands (Lee et
441 al., 2016; Selen et al., 2021). Using this mouse genetic model and a combination of next-
442 generation sequencing platforms we clarify the role for hepatic lipid content in metabolic gene
443 transcription, and in particular how Pparα, activated by natural ligands, maintains the
444 transcriptional architecture necessary for target gene expression (**Fig. 8**).

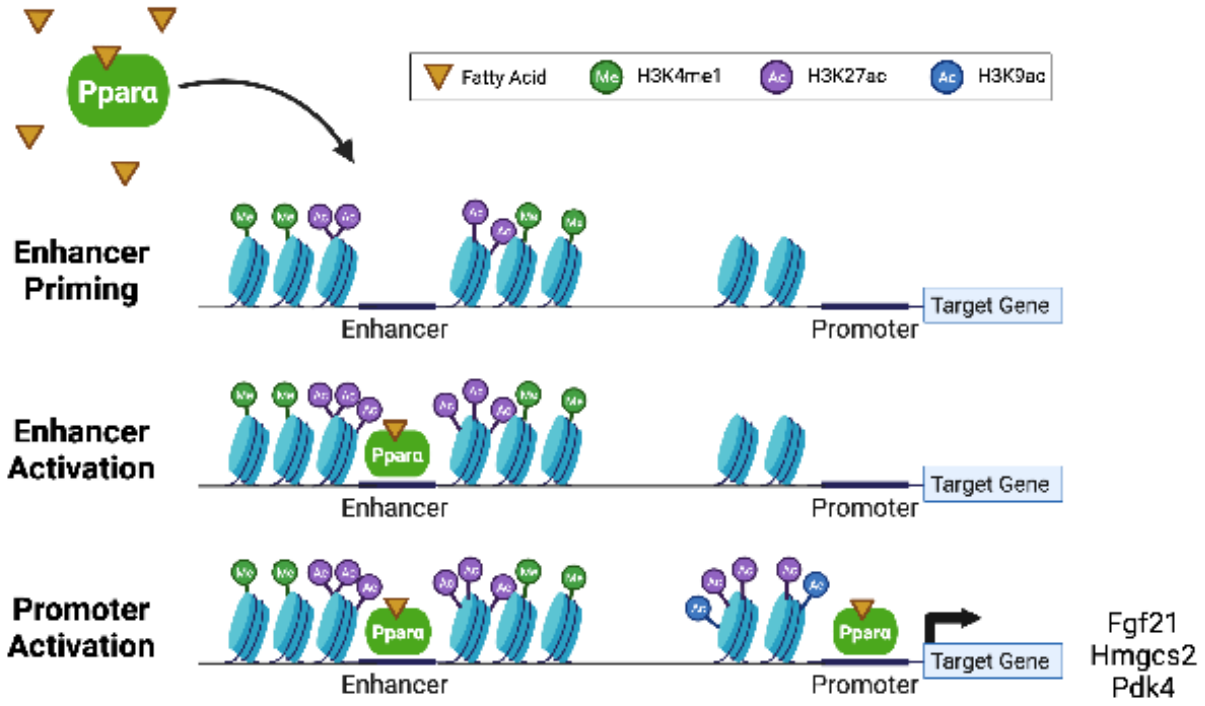

Fig 8. Pparα is required for lipid-responsive enhancer and promoter activation
Deficit in mitochondrial β-oxidation and/or excess fatty acids prompts H3K4me1 and H3K27ac deposition at lipid-responsive enhancer elements. This signals ligand-activated Pparα recruitment, and subsequent enhancer accessibility and activity. Pparα then binds to target gene promoters to drive chromatin acetylation, thereby inducing transcription of fatty acid catabolic genes to alleviate heightened lipid burden.

446 Our system benefits from use of *in vivo* metabolic perturbations to assess the role for
447 excess fatty acids in driving transcription. It has been stipulated that fatty acid oxidation
448 promotes transcription of metabolic genes via bulk increase to histone acetylation by lipid-
449 derived acetyl-CoA (McDonnell et al., 2016). Our data instead reveal that changes in hepatic
450 lipid levels can induce metabolic gene transcription even when mitochondrial β-oxidation, and
451 subsequent acetyl-CoA production, is inhibited. Indeed we detected no changes in bulk histone
452 acetylation in Cpt2$^{L-/-}$ liver. We instead observed that promoter acetylation patterns for many
453 lipid catabolic genes are Pparα-dependent. Enhancers displayed Pparα-independent
454 acetylation proximal to Pparα binding sites, but enhancer chromatin remained inaccessible in
455 the absence of the transcription factor. This indicates that fatty acid-induced transcription is
456 stimulated not by epigenetic changes, but instead by ligand-induced Pparα activation and the
457 associated chromatin remodeling. Studies in mice given a high fat diet (HFD) provide
458 supplemental evidence for our observations on fatty acid-driven transcription. In parallel with
459 our results, HFD-fed mice show increased hepatic lipid content as well as Pparα-dependent
460 hepatic gene expression (Patsouris et al., 2006). HFD-fed mice likewise exhibit suppressed
461 liver acetyl-CoA content but no difference in bulk histone acetylation compared to chow-fed
462 controls (Carrer et al., 2017).
463 A common method to stimulate Pparα and define target genes is to use a
464 pharmacological agonist (Brocker et al., 2020; Janssen et al., 2015; Lee et al., 1995;
465 Rakhshandehroo et al., 2007). Here we instead use fasting-induced buildup of endogenous
466 ligand to activate Pparα. We observed two distinct patterns of target gene transcription. In the
467 first group (Cluster 1), target genes require Pparα for promoter accessibility and acetylation
468 under conditions of high lipid availability. In the second group (Cluster 3), target genes do not
469 require Pparα for promoter acetylation. Promoter accessibility for the latter cluster is maintained
470 in Pparα$^{-/-}$ animals, though to a lesser extent than measured in WT controls. We therefore

471 hypothesize that a secondary mechanism maintains transcriptionally permissive H3K27ac
472 occupancy at these loci independent of Pparα, thereby promoting baseline gene expression.
473 The additional requirement of Pparα for gene induction above baseline is reflected in both the
474 RNA-seq and ATAC-seq datasets.

475 Cluster 3 gene promoters are enriched for the Hnf4α biding motif, suggesting the nuclear
476 hormone receptor may be involved in Pparα-independent promoter acetylation. It should be
477 noted that Hnf4α can bind directly to promoter sequences of *Fgf21*, *Hmgcs2*, and *Cpt1* to
478 obstruct Pparα binding and gene transcription (Martinez-Jimenez et al., 2010). However, these
479 three genes were assigned to Cluster 1, leaving open the possibility of Hnf4α involvement in
480 Cluster 3 promoter activation. Hnf4α is highly expressed in the three knockout genotypes,
481 providing additional evidence for this suggestion. We similarly observe high incidence of Hnf4α
482 motifs at active enhancers, in line with previous work demonstrating that Hnf4α maintains
483 H3K27ac occupancy at active enhancers in mouse liver (Thakur et al., 2019).

484 Previous *in vivo* work has advanced a role for Pparα localization to hepatic enhancers.
485 In a model of diet induced obesity, Pparα-null mice had suppressed circadian transcription for
486 eRNA proximal to Pparα binding motifs (Guan et al., 2018). In another study, hepatic fed state
487 Pparα ChIP-seq binding sites were observed to overlap with fasting-induced enhancers
488 (Goldstein et al., 2017). Our research builds upon those observations by demonstrating that
489 Pparα-sensitive enhancer elements in fasting liver are associated with lipid signaling. Elevated
490 enhancer accessibility in $Cpt2^{L-/-}$ animals, including particularly high ATAC-seq signal over
491 Pparα binding sites, further indicates that lipids drive Pparα engagement with active chromatin.
492 Moreover, depleted chromatin accessibility over all active enhancers in Pparα-null animals
493 indicates the requirement of Pparα to properly maintain the hepatic fasting enhancer landscape.

494 It's notable that Pparα loss does not significantly impact global enhancer epigenetic
495 state. Indeed, enhancer priming proximal to Pparα binding sites is independent of Pparα itself.

496 Increased H3K4me1 signal in DKO animals compared to other genotypes likely indicates a
497 compensatory signal to engage lipid-sensitive enhancers in response to the hepatocyte's need
498 for oxidative clearance of excess fatty acid. Enhancer H3K27ac signal adjacent to Pparα
499 binding sites is likewise globally independent of Pparα. Both $Cpt2^{L-/-}$ and DKO animals display
500 the highest levels of enhancer acetylation near Pparα binding sites, and yet these two
501 genotypes also display the lowest global enhancer H3K27ac signal. In other words, the $Cpt2^{L-/-}$
502 background drives enhancer acetylation specifically in proximity to Pparα binding sites,
503 providing evidence for a mechanism in which high lipid levels prompt H3K4me1 and H3K27ac
504 deposition to prime Pparα-sensitive enhancers, and credibly acting as a signal for Pparα DNA
505 binding.

506 While overall enhancer maintenance near Pparα binding sites is independent of Pparα,
507 insight into the Pparα enhancer program is gained by examining differential comparisons
508 between genotypes. One striking observation was that Pparα-associated H3K27ac signal
509 changes occurred more frequently in enhancer elements compared to promoters. $Cpt2^{L-/-}$-
510 associated lipid prompts an H3K27ac ChIP-seq signal increase at 5.5x more enhancers than
511 promoters. Similarly, loss of Pparα in Class B enhancers (DKO < $Cpt2^{L-/-}$) is associated with
512 H3K27ac signal depletion at 3.7x more enhancers than promoters. Finally, $Pparα^{-/-}$ animals
513 show H3K27ac depletion at 1.7x more enhancers than promoters. This notable degree of signal
514 change at enhancer regions, combined with the high incidence of Pparα binding sites and
515 association with GREAT lipid metabolism ontology terms, suggests that Pparα effects more
516 transcriptionally influential changes to chromatin architecture at enhancers over promoters. We
517 believe this indicates that the mechanism for adjusting Pparα target gene transcription levels is
518 more closely linked to enhancer remodeling than to promoter dynamics.

519 These expanded insights into Pparα gene regulation provide evidence for discrete
520 modes by which the liver signals its transcriptional needs in the face of metabolic perturbations

521 linked to fluctuations in lipid availability. We demonstrate distinct types of Pparα signaling
522 based on patterns of chromatin state and transcriptional output, show the role for Pparα in
523 hepatic enhancer maintenance, and further suggest secondary mechanisms which aid and
524 potentially even modulate Pparα signaling. These data prompt questions as to what role Pparα
525 may play in regulating the transcriptional landscape associated with lipid sensing in other
526 tissues, such as the kidney and adipose. This study thus uncovers new avenues of
527 investigation into lipid sensing at the levels of locus-specificity, tissue-specificity, and broader
528 metabolic physiology.
529

530 **MATERIALS & METHODS**

531 **Animals**

532 All procedures were performed in accordance with the NIH's Guide for the Care and Use of
533 Laboratory Animals and under the approval of the Johns Hopkins School of Medicine Animal
534 Care and Use Committee.
535

536 $Cpt2^{fl/fl}$ and Albumin-Cre;$Cpt2^{fl/fl}$ ($Cpt2^{L-/-}$) mice were previously described (Lee et al., 2015,
537 2016). $Cpt2^{fl/fl}$;Ppar$\alpha^{-/-}$ and $Cpt2^{L-/-}$;Ppar$\alpha^{-/-}$ animals were generated by initially crossing $Cpt2^{fl/fl}$ or
538 $Cpt2^{L-/-}$ animals with Ppar$\alpha^{-/-}$ mice (Jackson Laboratories; stock no. 008154). Mice for
539 experiments were bred from either $Cpt2^{fl/fl}$ crossed to $Cpt2^{L-/-}$ animals or $Cpt2^{fl/fl}$;Ppar$\alpha^{-/-}$ crossed
540 to $Cpt2^{L-/-}$;Ppar$\alpha^{-/-}$ animals. All mice were housed in a facility with ventilated racks on a 14h
541 light/10h dark cycle with *ad libitum* access to a standard rodent chow (2018SX Teklad Global,
542 18% protein). For fasting experiments, 9 week old male mice were deprived of food for 24 hours
543 (3p.m.-3 p.m). Tissues and serum were collected and flash-frozen at time of harvest.
544

545 **Immunoblotting**

546 Flash-frozen liver tissue was homogenized in RIPA buffer (50 mM Tris-HCl at pH 7.4, 150 mM
547 NaCl, 1 mM EDTA, 1% Triton X-100, and 0.25% deoxycholate) with PhosSTOP phosphatase
548 Inhibitor (Roche) and protease inhibitor cocktail (Roche). Homogenates were rotated for 30
549 minutes at 4°C and then centrifuged at 18,000g for 15 minutes. Total protein concentrations
550 were quantified by BCA assay (Thermo Fisher Scientific).
551
552 Protein lysates (30ug input) were separated by Tris-glycine SDS-PAGE (10-12% polyacrylamide
553 gels), followed by a transfer to PVDF membranes (Immobilon). Membranes were blocked with
554 5% nonfat milk in TBST for 1 hour and incubated overnight at 4°C with primary antibodies at
555 1:1000 in 3% BSA in TBST: Acetylated-Lysine, 9441, Cell Signaling Technologies; Histone H3,
556 4499, Cell Signaling Technology, Acetyl-Histone H3 Lys9, 9649, Cell Signaling Technologies;
557 Acetyl-Histone H3 Lys14, 7627, Cell Signaling Technologies; HSC70, 7298, Santa Cruz
558 Biotechnology. HRP-conjugated anti-rabbit (Cytiva, NA934V) or fluorescence-based (Cy3-
559 conjugated anti-mouse or Cy5-conjugated anti-rabbit; Invitrogen, Thermo Fisher Scientific)
560 secondaries were used at 1:1000. Blots were imaged using the Amersham Prime enhanced
561 chemiluminescent substrate (Cytiva) or epifluorescence on an Alpha Innotech MultiImage III
562 instrument.
563
564 Histones were acid precipitated as previously described using an overnight 0.4N H_2SO_4
565 incubation and 1 hour TCA precipitation (Shechter et al., 2007). Histones were visualized per
566 above using 15ug protein input on an 8% polyacrylamide gel.
567
568 **Mass Spectrometry & Proteomic Analysis**
569 Flash-liver tissue was submitted to the Johns Hopkins Center for Proteomics Core for total
570 proteome and acetyl-proteome analysis. Samples were prepared in lysis buffer with 8M urea
571 and 50mM tetraethyl ammoniumbicarbonate. Lysates were treated with LysC and trypsin, then

572 labeled with 10-plex TMT. Peptide fractionation was done using basic pH reverse phase liquid
573 chromatography, resulting in 24 fractions. Fractions were analyzed using an Orbitrap Fusion
574 Lumos (Thermo Scientific) on an Easy nLC 1200 (Thermo Scientific) using MS1 resolution =
575 120,000 and MS2 resolution = 30,000, HCD fragmentation method, and MS2 collision energy =
576 35. Each fraction received a two hour run time.
577
578 Total proteome analysis was done in Perseus (version 1.6.0.0) (Cox and Mann, 2012). p-value
579 was calculated by Student's t-test. q-value was calculated by significance analysis of
580 microarrays (SAM) and permutation based false discovery rate (FDR), with SAM S0 value = 0.1
581 (Tusher et al., 2001).
582
583 Acetyl-proteome was analyzed with Proteome Discoverer 2.1 (Thermo Scientific) using RefSeq
584 version 78. The following parameters were used: cleavage enzyme was set as trypsin, no more
585 than five missed cleavages were allowed, fixed modification was carbamidomethyl on cysteine
586 residue, dynamic modifications were acetyl group on protein N-terminus or oxidation on
587 methionine and acetyl-lysine, and MS2 level quantification. A 1% FDR was applied for both
588 peptide and protein levels. Acetyl-proteome data were normalized to median of total proteome
589 to remove systemic deviation.
590
591 The COMPARTMENT dataset was used to assign localization for peptides for all cell
592 compartments except mitochondria (Binder et al., 2014). Only COMPARTMENTS annotations
593 with a minimum confidence score of 3 were used. Mitochondrial peptides were assigned using
594 the MitoCarta 2.0 (Calvo et al., 2016).
595
596 **Tissue acetyl-CoA**

597 Flash-frozen liver tissue was submitted to the Mouse Metabolic Phenotyping Center at Case
598 Western Reserve University for acetyl-CoA measurements via liquid chromatography-mass
599 spectrometry.
600
601 **Serum metabolites**
602 Blood glucose levels in fasted mice were measured at time of harvest using a Nova Max Plus
603 glucometer.
604
605 Untargeted metabolomics on serum was performed by Metabolon Inc (n=6). For analysis raw
606 area counts for each biochemical species were rescaled to set the median equal to 1. Heatmap
607 and PCA were generated by MetaboAnalyst (Chong et al., 2019). Differentially regulated
608 metabolites for heatmap were determined using a 1-way ANOVA with Fisher's LSD.
609
610 **RNA-sequencing library preparation**
611 Total RNA was isolated from flash-frozen liver tissue was using TRIzol reagent (Invitrogen,
612 Thermo Fisher Scientific), followed by addition purification using RNeasy Mini Kit (QIAGEN), per
613 manufacturer recommendations. RNA quality was assessed by Nanodrop.
614
615 RNA was then submitted to Novogene Corporation Inc (China & Davis, CA, USA) for library
616 construction and sequencing. Four biological replicates were used for each genotype. Reads
617 were aligned to mouse reference genome (mm10) using STAR software (Dobin et al., 2013).
618 Investigators performed analyses downstream of read count acquisition.
619
620 **RNA-seq Analysis**
621 Differential expression was performed on raw read counts in R with DESeq2 (v3.12) using the
622 Wald test with betaPrior=FALSE and lfcShrink type="apeglm" (Love et al., 2014; Zhu et al.,

623 2019). Differential expression cutoff was fold change ≥ |2|, padj < 0.05. Normalized read counts
624 were visualized in GraphPad Prism. PCA plot was generated using pcaExlorer package (Marini
625 and Binder, 2019). WY14643-responsive genes were determined from GSE140063 using the
626 same differential expression pipeline (Naiman et al., 2019).
627
628 K-means clustering of differentially expressed transcripts was performed in R on rlog
629 transformed count values from DESeq2 output. Optimal cluster number (n=5) was determined
630 by gap statistic (factoextra package). K-means clustering was performed and visualized in the
631 pheatmap package with Z-score row scaling [$(x - \bar{x})/\sigma$]. Tracing diagrams were generated using
632 the ggplot2 package (Wickham, 2016). Gene ontology and KEGG pathway enrichment was
633 obtained using the DAVID web application (Huang et al., 2007).
634
635 **ATAC-seq and ChIP-seq library preparation**
636 ATAC-seq and ChIP-seq were performed using Active Motif sequencing services (Carlsbad,
637 CA). Flash-frozen liver tissue was submitted to Active Motif, with two biological replicates per
638 genotype for H3K4me1 and H3K27ac ChIP-seq, and ATAC-seq. One biological replicate was
639 submitted for H3K9ac ChIP-seq. Library construction was performed according to company
640 protocol. The following antibodies were used for ChIP-seq: H3K4me1 (Active Motif #39297),
641 H3K9ac (Active Motif #39917), H3K27ac (Active Motif #39133).
642
643 **ATAC-Seq & ChIP-seq Analysis**
644 Sequence acquisition, mapping, raw BAM file generation, and peak calling was performed by
645 Active Motif. For ATAC-seq, paired-end 42nt sequencing reads generated by Illumina NexSeq
646 500 were mapped to mm10 reference genome using the BWA algorithm with default settings (Li
647 and Durbin, 2009). For ChIP-seq, single-end 75nt sequencing reads generated by Illumina
648 NexSeq 500 were mapped to mm10 reference genome using the BWA algorithm with

649 “bwaln/samse” default settings. For normalization, tag number of all samples within a
650 comparison group was reduced by random down-sampling to the number of tags present in the
651 smallest sample. Peak calling was performed using MACS2 with default cutoff values (Zhang et
652 al., 2008); ATAC-seq paired reads were treated as independent events. ENCODE blacklist
653 regions were removed (Amemiya et al., 2019). bigWig files for visualization on UCSC Genome
654 Browser were created using a 32nt bin with a 200bp *in silico* tag extension (Kent et al., 2002).
655 Investigators performed downstream analysis.
656
657 Raw BAM files were processed using samtools and bamtools to remove reads with mapq score
658 < 25, unmapped reads, mitochondrial reads, and reads with more than 2 mismatches (Barnett
659 et al., 2011; Li et al., 2009). Aggregation plots and motif analysis were generated
660 using Hypergeometric Optimization of Motif EnRichment (HOMER) (Heinz et al., 2010). Motif
661 analysis was calculated using ‘findMotifsGenome.pl’ with -size 500 on BED file input with that
662 assumption that a broad scanning window is preferred for histone mark motif analysis.
663 knownResults motif output are reported in this study. Tag directories for histograms were
664 generated from BAM files using ‘makeTagDirectory.pl’ with -fragLength 200 and -tbp 1. Tag
665 directories combined both biological replicates per genotype. Aggregation plots were produced
666 using ‘annotatePeaks.pl’ with -hist 10 and normalization set to the lowest sample tag count
667 within a comparison group. Plots and corresponding bar charts, reported as tags per bp per
668 peak, were visualized in GraphPad Prism 9.
669
670 Diffbind (v3.13) was used to generate a RangedSummarizedExperiment from BAM and
671 narrowPeak files with the following parameters: fragmentLength=200,
672 score=DBA_SCORE_READS, summits=TRUE, bUseSummarizeOverlaps=FALSE,
673 bRemoveDuplicates=TRUE, and minOverlap=2 (Ross-Innes et al., 2012; Stark and Brown,
674 2011). mm10 ENCODE blacklist regions were removed by calling dba.blacklist(). Default

675 normalization with full library size was called with dba.normalize(). ATAC-seq normalization
676 included background=TRUE due to large changes between genotypes.
677 RangedSummarizedExperiment was passed to DESeq2 for differential peak analysis using
678 betaPrior=TRUE. Significance cutoff for differential peak analysis was considered fold change ≥
679 |2|, padj < 0.05. ATAC-seq MA plots were generated in Diffbind. PCA plots were generated
680 using pcaExlorer on DESeq2 rlog transformed read counts.
681
682 **Enhancer Analysis**
683 All genome arithmetic to compare peak coordinates was done using bedtools (Quinlan, 2014;
684 Quinlan and Hall, 2010). This study only focused on active enhancer elements that were
685 detected in one or more genotypes; regions enriched for H3K4me1 alone were excluded. Active
686 enhancers were defined as a region with H3K4me1 and H3K27ac co-occupancy excluding
687 intervals located within 2kb of a transcription start site or termination site (Calo and Wysocka,
688 2013; Creyghton et al., 2010). Chromatin accessibility was not used to define active enhancers
689 due to the severe global depletion in ATAC-seq tag density observed in Pparα-null animals.
690 Gene coordinates were obtained from the UCSC Table Browser refGene (2020-08-17 update)
691 (Karolchik et al., 2004). H3K4me1 and H3K27ac overlap was determined with a minimum 50%
692 H3K27ac interval overlap over an H3K4me1 peak due to account for differences in histone mark
693 average peak length. Fasting liver Pparα ChIP-seq coordinates were obtained from GSE118788
694 (Supplementary File Pparα-C57-Fast-peaks) (Sommars et al., 2019).
695
696 Differential enhancer groups were defined using the H3K27ac ChIP-seq DESeq2 output from
697 above with the significance cutoff set at fold change ≥ |2|, padj < 0.05. DESeq2 normalized
698 values were used for enhancer tag counts. Enhancer heatmaps were generated from bigWig
699 files using deepTools 2.0 with 'computeMatrix' reference-point mode and 'plotHeatmap'
700 (Ramírez et al., 2016).

701

702 Enhancer ontology was determined with the Genomic Regions Enrichment of Annotations Tool
703 (GREAT) (McLean et al., 2010). GREAT version 4.0.4 was used in “basal plus extension” mode
704 with default parameters and a 500kb maximum extension. Curated regulatory domains were
705 included in calculations.

706

707 **Statistical Analysis**

708 All statistical comparisons were carried out in GraphPad Prism 9 unless otherwise noted.
709 Significance was determined using Student’s t-test, 1-way ANOVA with Tukey’s post hoc
710 correction, or Kruskal-Wallis test with Dunn’s post hoc correction as noted. Shapiro-Wilk test for
711 normality was used in R to determine whether to use a parametric or non-parametric test for
712 significance for genomic data.

713

714 **DATA AND SOFTWARE AVAILABILITY**

715 RNA-seq data were deposited in GSE165701. ChIP-seq and ATAC-seq data were deposited in
716 GEO SuperSeries GSE179053. Scripts used for RNA-seq, ChIP-seq, and ATAC-seq analysis
717 can be found at https://github.com/WolfgangLabJHMI/cpt2_ppara_liver_seq. The mass
718 spectrometry proteomics data have been deposited to the ProteomeXchange Consortium via
719 the PRIDE partner repository with the dataset identifier PXD027235.

720

721 **ACKNOWLEDGEMENTS**

722 This work was supported in part by a National Institutes of Health grant R01DK120530 and
723 R01DK116746 to M.J.W.

724

725 We thank Dr. Caitlyn Bowman-Cornelius for initial mouse breeding, Dr. Ebru Selen for advice on
726 metabolomics analysis, and Dr. Anastasia Kralli for helpful conversations. We also thank Dr.

Chan-Hyun Na and the Johns Hopkins Center for Proteomics Discovery for proteomic data acquisition.

AUTHOR CONTRIBUTIONS

M.J.W and K.S.C conceptualized the project. K.S.C collected and analyzed data. K.S.C and M.J.W participated in the writing, review, and editing of the manuscript.

REFERENCES

Amemiya, H.M., Kundaje, A., and Boyle, A.P. (2019). The ENCODE Blacklist: Identification of Problematic Regions of the Genome. Scientific Reports *9*, 1–5.

Andersson, R., and Sandelin, A. (2020). Determinants of enhancer and promoter activities of regulatory elements. Nature Reviews Genetics *21*, 71–87.

Aoyama, T., Peters, J.M., Iritani, N., Nakajima, T., Furihata, K., Hashimoto, T., and Gonzalez, F.J. (1998). Altered constitutive expression of fatty acid-metabolizing enzymes in mice lacking the peroxisome proliferator-activated receptor α (PPARα). Journal of Biological Chemistry *273*, 5678–5684.

Asrani, S.K., Devarbhavi, H., Eaton, J., and Kamath, P.S. (2019). Burden of liver diseases in the world. Journal of Hepatology *70*, 151–171.

Bardot, O., Aldridge, T.C., Latruffe, N., and Green, S. (1993). PPAR-RXR heterodimer activates a peroxisome proliferator response element upstream of the bifunctional enzyme gene. Biochemical and Biophysical Research Communications *192*, 37–45.

Barnett, D.W., Garrison, E.K., Quinlan, A.R., Stŕmberg, M.P., and Marth, G.T. (2011). Bamtools: A C++ API and toolkit for analyzing and managing BAM files. Bioinformatics *27*, 1691–1692.

Binder, J.X., Pletscher-Frankild, S., Tsafou, K., Stolte, C., O'Donoghue, S.I., Schneider, R., and Jensen, L.J. (2014). COMPARTMENTS: Unification and visualization of protein subcellular localization evidence. Database *2014*, bau012–bau012.

Boergesen, M., Pedersen, T.A., Gross, B., van Heeringen, S.J., Hagenbeek, D., Bindesboll, C., Caron, S., Lalloyer, F., Steffensen, K.R., Nebb, H.I., et al. (2012). Genome-Wide Profiling of Liver X Receptor, Retinoid X Receptor, and Peroxisome Proliferator-Activated Receptor in Mouse Liver Reveals Extensive Sharing of Binding Sites. Molecular and Cellular Biology

758 *32*, 852–867.
759 Bowman, C.E., Selen Alpergin, E.S., Cavagnini, K., Smith, D.M., Scafidi, S., and Wolfgang, M.J.
760 (2019). Maternal Lipid Metabolism Directs Fetal Liver Programming following Nutrient
761 Stress. Cell Reports *29*.
762 Brocker, C.N., Kim, D., Melia, T., Karri, K., Velenosi, T.J., Takahashi, S., Aibara, D., Bonzo,
763 J.A., Levi, M., Waxman, D.J., et al. (2020). Long non-coding RNA Gm15441 attenuates
764 hepatic inflammasome activation in response to PPARA agonism and fasting. Nature
765 Communications *11*.
766 Calo, E., and Wysocka, J. (2013). Modification of Enhancer Chromatin: What, How, and Why?
767 Molecular Cell *49*, 825–837.
768 Calvo, S.E., Clauser, K.R., and Mootha, V.K. (2016). MitoCarta2.0: An updated inventory of
769 mammalian mitochondrial proteins. Nucleic Acids Research *44*, D1251–D1257.
770 Carrer, A., Parris, J.L.D., Trefely, S., Henry, R.A., Montgomery, D.C., Torres, A., Viola, J.M.,
771 Kuo, Y.M., Blair, I.A., Meier, J.L., et al. (2017). Impact of a high-fat diet on tissue Acyl-CoA
772 and histone acetylation levels. Journal of Biological Chemistry *292*, 3312–3322.
773 Chong, J., Wishart, D.S., and Xia, J. (2019). Using MetaboAnalyst 4.0 for Comprehensive and
774 Integrative Metabolomics Data Analysis. Current Protocols in Bioinformatics *68*, e86.
775 Cox, J., and Mann, M. (2012). 1D and 2D annotation enrichment: a statistical method integrating
776 quantitative proteomics with complementary high-throughput data. BMC Bioinformatics *13*
777 *Suppl 16*, 1–11.
778 Creyghton, M.P., Cheng, A.W., Welstead, G.G., Kooistra, T., Carey, B.W., Steine, E.J., Hanna,
779 J., Lodato, M.A., Frampton, G.M., Sharp, P.A., et al. (2010). Histone H3K27ac separates
780 active from poised enhancers and predicts developmental state. Proceedings of the
781 National Academy of Sciences of the United States of America *107*, 21931–21936.
782 Dobin, A., Davis, C.A., Schlesinger, F., Drenkow, J., Zaleski, C., Jha, S., Batut, P., Chaisson,
783 M., and Gingeras, T.R. (2013). STAR: Ultrafast universal RNA-seq aligner. Bioinformatics
784 *29*, 15–21.
785 Evans, R.M., and Mangelsdorf, D.J. (2014). Nuclear receptors, RXR, and the big bang. Cell
786 *157*, 255–266.
787 Francque, S., Verrijken, A., Caron, S., Prawitt, J., Paumelle, R., Derudas, B., Lefebvre, P.,
788 Taskinen, M.R., Van Hul, W., Mertens, I., et al. (2015). PPARα gene expression correlates
789 with severity and histological treatment response in patients with non-alcoholic
790 steatohepatitis. Journal of Hepatology *63*, 164–173.
791 Gearing, K.L., Gottlicher, M., Teboul, M., Widmark, E., and Gustafsson, J.A. (1993). Interaction

792 of the peroxisome-proliferator-activated receptor and retinoid X receptor. Proceedings of
793 the National Academy of Sciences of the United States of America *90*, 1440–1444.
794 George, F.C. (2006). Fuel metabolism in starvation. Annual Review of Nutrition *26*, 1–22.
795 Goldstein, I., and Hager, G.L. (2015). Transcriptional and Chromatin Regulation during Fasting -
796 The Genomic Era. Trends in Endocrinology and Metabolism *26*, 699–710.
797 Goldstein, I., Baek, S., Presman, Di.M., Paakinaho, V., Swinstead, E.E., and Hager, G.L.
798 (2017). Transcription factor assisted loading and enhancer dynamics dictate the hepatic
799 fasting response. Genome Research *27*, 427–439.
800 Gong, Z., Tas, E., Yakar, S., and Muzumdar, R. (2017). Hepatic lipid metabolism and non-
801 alcoholic fatty liver disease in aging. Molecular and Cellular Endocrinology *455*, 115–130.
802 Greenberg, A.S., Coleman, R.A., Kraemer, F.B., McManaman, J.L., Obin, M.S., Puri, V., Yan,
803 Q.W., Miyoshi, H., and Mashek, D.G. (2011). The role of lipid droplets in metabolic disease
804 in rodents and humans. Journal of Clinical Investigation *121*, 2102–2110.
805 Guan, D., Xiong, Y., Borck, P.C., Jang, C., Doulias, P.T., Papazyan, R., Fang, B., Jiang, C.,
806 Zhang, Y., Briggs, E.R., et al. (2018). Diet-Induced Circadian Enhancer Remodeling
807 Synchronizes Opposing Hepatic Lipid Metabolic Processes. Cell *174*, 831-842.e12.
808 Heinz, S., Benner, C., Spann, N., Bertolino, E., Lin, Y.C., Laslo, P., Cheng, J.X., Murre, C.,
809 Singh, H., and Glass, C.K. (2010). Simple Combinations of Lineage-Determining
810 Transcription Factors Prime cis-Regulatory Elements Required for Macrophage and B Cell
811 Identities. Molecular Cell *38*, 576–589.
812 Heinz, S., Romanoski, C.E., Benner, C., and Glass, C.K. (2015). The selection and function of
813 cell type-specific enhancers. Nature Reviews Molecular Cell Biology *16*, 144–154.
814 Houten, S.M., Violante, S., Ventura, F. V., and Wanders, R.J.A. (2016). The Biochemistry and
815 Physiology of Mitochondrial Fatty Acid β-Oxidation and Its Genetic Disorders. Annual
816 Review of Physiology *78*, 23–44.
817 Huang, B., Wu, P., Bowker-Kinley, M.M., and Harris, R.A. (2002). Regulation of pyruvate
818 dehydrogenase kinase expression by peroxisome proliferator-activated receptor-α ligands,
819 glucocorticoids, and insulin. Diabetes *51*, 276–283.
820 Huang, D.W., Sherman, B.T., Tan, Q., Kir, J., Liu, D., Bryant, D., Guo, Y., Stephens, R.,
821 Baseler, M.W., Lane, H.C., et al. (2007). DAVID Bioinformatics Resources: Expanded
822 annotation database and novel algorithms to better extract biology from large gene lists.
823 Nucleic Acids Research *35*.
824 Inagaki, T., Dutchak, P., Zhao, G., Ding, X., Gautron, L., Parameswara, V., Li, Y., Goetz, R.,
825 Mohammadi, M., Esser, V., et al. (2007). Endocrine Regulation of the Fasting Response by

826 PPARα-Mediated Induction of Fibroblast Growth Factor 21. Cell Metabolism *5*, 415–425.
827 Iroz, A., Montagner, A., Benhamed, F., Levavasseur, F., Polizzi, A., Anthony, E., Régnier, M.,
828 Fouché, E., Lukowicz, C., Cauzac, M., et al. (2017). A Specific ChREBP and PPARα
829 Cross-Talk Is Required for the Glucose-Mediated FGF21 Response. Cell Reports *21*, 403–
830 416.
831 Janssen, A.W.F., Betzel, B., Stoopen, G., Berends, F.J., Janssen, I.M., Peijnenburg, A.A., and
832 Kersten, S. (2015). The impact of PPARaα activation on whole genome gene expression in
833 human precision cut liver slices. BMC Genomics *16*.
834 Jump, D.B., Tripathy, S., and Depner, C.M. (2013). Fatty acid-regulated transcription factors in
835 the liver. Annual Review of Nutrition *33*, 249–269.
836 Karagianni, P., and Talianidis, I. (2015). Transcription factor networks regulating hepatic fatty
837 acid metabolism. Biochimica et Biophysica Acta - Molecular and Cell Biology of Lipids
838 *1851*, 2–8.
839 Karolchik, D., Hinricks, A.S., Furey, T.S., Roskin, K.M., Sugnet, C.W., Haussler, D., and Kent,
840 W.J. (2004). The UCSC table browser data retrieval tool. Nucleic Acids Research *32*.
841 Kent, W.J., Sugnet, C.W., Furey, T.S., Roskin, K.M., Pringle, T.H., Zahler, A.M., and Haussler,
842 a. D. (2002). The Human Genome Browser at UCSC. Genome Research *12*, 996–1006.
843 Kersten, S. (2014). Integrated physiology and systems biology of PPARα. Molecular Metabolism
844 *3*, 354–371.
845 Kersten, S., Seydoux, J., Peters, J.M., Gonzalez, F.J., Desvergne, B., and Wahli, W. (1999).
846 Peroxisome proliferator-activated receptor α mediates the adaptive response to fasting.
847 Journal of Clinical Investigation *103*, 1489–1498.
848 Kersten, S., Rakhshandehroo, M., Knoch, B., and Müller, M. (2010). Peroxisome proliferator-
849 activated receptor alpha target genes. PPAR Research.
850 Lee, J., Ellis, J.M., and Wolfgang, M.J. (2015). Adipose fatty acid oxidation is required for
851 thermogenesis and potentiates oxidative stress-induced inflammation. Cell Reports *10*,
852 266–279.
853 Lee, J., Choi, J., Scafidi, S., and Wolfgang, M.J. (2016). Hepatic Fatty Acid Oxidation Restrains
854 Systemic Catabolism during Starvation. Cell Reports *16*, 201–212.
855 Lee, J.M., Wagner, M., Xiao, R., Kim, K.H., Feng, D., Lazar, M.A., and Moore, D.D. (2014).
856 Nutrient-sensing nuclear receptors coordinate autophagy. Nature *516*, 112–115.
857 Lee, S.S., Pineau, T., Drago, J., Lee, E.J., Owens, J.W., Kroetz, D.L., Fernandez-Salguero,
858 P.M., Westphal, H., and Gonzalez, F.J. (1995). Targeted disruption of the alpha isoform of
859 the peroxisome proliferator-activated receptor gene in mice results in abolishment of the

860 pleiotropic effects of peroxisome proliferators. Molecular and Cellular Biology *15*, 3012–
861 3022.
862 Leone, T.C., Weinheimer, C.J., and Kelly, D.P. (1999). A critical role for the peroxisome
863 proliferator-activated receptor α (PPARα) in the cellular fasting response: The PPARα-null
864 mouse as a model of fatty acid oxidation disorders. Proceedings of the National Academy
865 of Sciences of the United States of America *96*, 7473–7478.
866 Li, H., and Durbin, R. (2009). Fast and accurate short read alignment with Burrows-Wheeler
867 transform. Bioinformatics *25*, 1754–1760.
868 Li, G., Brocker, C.N., Xie, C., Yan, T., Noguchi, A., Krausz, K.W., Xiang, R., and Gonzalez, F.J.
869 (2018). Hepatic peroxisome proliferator-activated receptor alpha mediates the major
870 metabolic effects of Wy-14643. Journal of Gastroenterology and Hepatology (Australia) *33*,
871 1138–1145.
872 Li, H., Handsaker, B., Wysoker, A., Fennell, T., Ruan, J., Homer, N., Marth, G., Abecasis, G.,
873 and Durbin, R. (2009). The Sequence Alignment/Map format and SAMtools. Bioinformatics
874 *25*, 2078–2079.
875 Love, M.I., Huber, W., and Anders, S. (2014). Moderated estimation of fold change and
876 dispersion for RNA-seq data with DESeq2. Genome Biology *15*, 550.
877 Mandard, S., Müller, M., and Kersten, S. (2004). Peroxisome proliferator-activated receptor α
878 target genes. Cellular and Molecular Life Sciences *61*, 393–416.
879 Marini, F., and Binder, H. (2019). PcaExplorer: An R/Bioconductor package for interacting with
880 RNA-seq principal components. BMC Bioinformatics *20*, 1–8.
881 Martinez-Jimenez, C.P., Kyrmizi, I., Cardot, P., Gonzalez, F.J., and Talianidis, I. (2010).
882 Hepatocyte Nuclear Factor 4 Coordinates a Transcription Factor Network Regulating
883 Hepatic Fatty Acid Metabolism. Molecular and Cellular Biology *30*, 565–577.
884 McDonnell, E., Crown, S.B., Fox, D.B., Kitir, B., Ilkayeva, O.R., Olsen, C.A., Grimsrud, P.A., and
885 Hirschey, M.D. (2016). Lipids Reprogram Metabolism to Become a Major Carbon Source
886 for Histone Acetylation. Cell Reports *17*, 1463–1472.
887 McLean, C.Y., Bristor, D., Hiller, M., Clarke, S.L., Schaar, B.T., Lowe, C.B., Wenger, A.M., and
888 Bejerano, G. (2010). GREAT improves functional interpretation of cis-regulatory regions.
889 Nature Biotechnology *28*, 495–501.
890 Naiman, S., Huynh, F.K., Gil, R., Glick, Y., Shahar, Y., Touitou, N., Nahum, L., Avivi, M.Y.,
891 Roichman, A., Kanfi, Y., et al. (2019). SIRT6 Promotes Hepatic Beta-Oxidation via
892 Activation of PPARα. Cell Reports *29*, 4127-4143.e8.
893 Patsouris, D., Reddy, J.K., Müller, M., and Kersten, S. (2006). Peroxisome proliferator-activated

894 receptor α mediates the effects of high-fat diet on hepatic gene expression. Endocrinology
895 *147*, 1508–1516.
896 Ponziani, F.R., Pecere, S., Gasbarrini, A., and Ojetti, V. (2015). Physiology and pathophysiology
897 of liver lipid metabolism. Expert Review of Gastroenterology and Hepatology *9*, 1055–1067.
898 Qin, Y., Grimm, S.A., Roberts, J.D., Chrysovergis, K., and Wade, P.A. (2020). Alterations in
899 promoter interaction landscape and transcriptional network underlying metabolic adaptation
900 to diet. Nature Communications *11*, 1–16.
901 Quinlan, A.R. (2014). BEDTools: The Swiss-Army tool for genome feature analysis. Current
902 Protocols in Bioinformatics *2014*, 11.12.1-11.12.34.
903 Quinlan, A.R., and Hall, I.M. (2010). BEDTools: A flexible suite of utilities for comparing genomic
904 features. Bioinformatics *26*, 841–842.
905 Raisner, R., Kharbanda, S., Jin, L., Jeng, E., Chan, E., Merchant, M., Haverty, P.M., Bainer, R.,
906 Cheung, T., Arnott, D., et al. (2018). Enhancer Activity Requires CBP/P300 Bromodomain-
907 Dependent Histone H3K27 Acetylation. Cell Reports *24*, 1722–1729.
908 Rakhshandehroo, M., Sanderson, L.M., Matilainen, M., Stienstra, R., Carlberg, C., De Groot,
909 P.J., Müller, M., and Kersten, S. (2007). Comprehensive analysis of PPARα-dependent
910 regulation of hepatic lipid metabolism by expression profiling. PPAR Research *2007*.
911 Rakhshandehroo, M., Hooiveld, G., Müller, M., and Kersten, S. (2009). Comparative Analysis of
912 Gene Regulation by the Transcription Factor PPARα between Mouse and Human. PLoS
913 ONE *4*, e6796.
914 Ramírez, F., Ryan, D.P., Grüning, B., Bhardwaj, V., Kilpert, F., Richter, A.S., Heyne, S., Dündar,
915 F., and Manke, T. (2016). deepTools2: a next generation web server for deep-sequencing
916 data analysis. Nucleic Acids Research *44*, W160–W165.
917 Reddy, J.K. (2001). Nonalcoholic steatosis and steatohepatitis III. Peroxisomal β-oxidation,
918 PPARα, and steatohepatitis. American Journal of Physiology - Gastrointestinal and Liver
919 Physiology *281*.
920 Ross-Innes, C.S., Stark, R., Teschendorff, A.E., Holmes, K.A., Ali, H.R., Dunning, M.J., Brown,
921 G.D., Gojis, O., Ellis, I.O., Green, A.R., et al. (2012). Differential oestrogen receptor binding
922 is associated with clinical outcome in breast cancer. Nature *481*, 389–393.
923 Ruppert, P.M.M., Park, J.G., Xu, X., Hur, K.Y., Lee, A.H., and Kersten, S. (2019).
924 Transcriptional profiling of PPARα-/- and CREB3L3-/- livers reveals disparate regulation of
925 hepatoproliferative and metabolic functions of PPARα. BMC Genomics *20*.
926 Selen, E.S., Choi, J., and Wolfgang, M.J. (2021). Discordant hepatic fatty acid oxidation and
927 triglyceride hydrolysis leads to liver disease. JCI Insight *6*.

928 Shechter, D., Dormann, H.L., Allis, C.D., and Hake, S.B. (2007). Extraction, purification and
929 analysis of histones. Nature Protocols *2*, 1445–1457.
930 Sommars, M.A., Ramachandran, K., Senagolage, M.D., Futtner, C.R., Germain, D.M., Allred,
931 A.L., Omura, Y., Bederman, I.R., and Barish, G.D. (2019). Dynamic repression by BCL6
932 controls the genome-wide liver response to fasting and steatosis. ELife *8*.
933 Song, S., Attia, R.R., Connaughton, S., Niesen, M.I., Ness, G.C., Elam, M.B., Hori, R.T., Cook,
934 G.A., and Park, E.A. (2010). Peroxisome proliferator activated receptor α (PPARα) and
935 PPAR gamma coactivator (PGC-1α) induce carnitine palmitoyltransferase IA (CPT-1A) via
936 independent gene elements. Molecular and Cellular Endocrinology *325*, 54–63.
937 Stark, R., and Brown, G. (2011). DiffBind: differential binding analysis of ChIP-Seq peak data.
938 http://bioconductor.org/packages/release/bioc/vignettes/DiffBind/inst/doc/DiffBind.pdf.
939 Stern, J.H., Rutkowski, J.M., and Scherer, P.E. (2016). Adiponectin, Leptin, and Fatty Acids in
940 the Maintenance of Metabolic Homeostasis through Adipose Tissue Crosstalk. Cell
941 Metabolism *23*, 770–784.
942 Thakur, A., Wong, J.C.H., Wang, E.Y., Lotto, J., Kim, D., Cheng, J.C., Mingay, M., Cullum, R.,
943 Moudgil, V., Ahmed, N., et al. (2019). Hepatocyte Nuclear Factor 4-Alpha Is Essential for
944 the Active Epigenetic State at Enhancers in Mouse Liver. Hepatology *70*, 1360–1376.
945 The, B., and Schulz, H. (1991). Beta oxidation of fatty acids. Biochimica et Biophysica Acta
946 (BBA) - Lipids and Lipid Metabolism *1081*, 109–120.
947 Tusher, V.G., Tibshirani, R., and Chu, G. (2001). Significance analysis of microarrays applied to
948 the ionizing radiation response. Proceedings of the National Academy of Sciences of the
949 United States of America *98*, 5116–5121.
950 Wickham, H. (2016). ggplot2: Elegant Graphics for Data Analysis (New York: Springer-Verlag).
951 Wu, P., Peters, J.M., and Harris, R.A. (2001). Adaptive increase in pyruvate dehydrogenase
952 kinase 4 during starvation is mediated by peroxisome proliferator-activated receptor α.
953 Biochemical and Biophysical Research Communications *287*, 391–396.
954 Zhang, Y., Liu, T., Meyer, C.A., Eeckhoute, J., Johnson, D.S., Bernstein, B.E., Nussbaum, C.,
955 Myers, R.M., Brown, M., Li, W., et al. (2008). Model-based analysis of ChIP-Seq (MACS).
956 Genome Biology *9*, R137.
957 Zhu, A., Ibrahim, J.G., and Love, M.I. (2019). Heavy-Tailed prior distributions for sequence
958 count data: Removing the noise and preserving large differences. Bioinformatics *35*, 2084–
959 2092.
960